

# The CLAS12 Ring Imaging Cherenkov Detector

M. Contalbrigo<sup>a</sup>, V. Kubarovský<sup>f</sup>, M. Mirazita<sup>b</sup>, P. Rossi<sup>f,b</sup>, G. Angelini<sup>b,j</sup>, H. Avakian<sup>f</sup>, K. Bailey<sup>g</sup>, I. Balossino<sup>a</sup>, L. Barion<sup>a</sup>, F. Benmokhtar<sup>h</sup>, P. Bonneau<sup>f</sup>, W. Briscoe<sup>i</sup>, W. Brooks<sup>k</sup>, E. Cisbani<sup>c</sup>, C. Cuevas<sup>f</sup>, P. Degtiarenko<sup>f</sup>, C. Dickover<sup>f</sup>, K. Hafidi<sup>g</sup>, K. Joo<sup>i</sup>, A. Kim<sup>i</sup>, T. Lemon<sup>f</sup>, V. Lucherini<sup>b</sup>, R. Malagutti<sup>a</sup>, R. Montgomery<sup>b</sup>, A. Movsisyan<sup>a</sup>, P. Musico<sup>d</sup>, T. O'Connor<sup>g</sup>, D. Orecchini<sup>b</sup>, L.L. Pappalardo<sup>a</sup>, C. Pecar<sup>h</sup>, R. Perrino<sup>e</sup>, B. Raydo<sup>f</sup>, S. Tomassini<sup>b</sup>, M. Turisini<sup>a,b</sup>, A. Yegneswaran<sup>f</sup>

<sup>a</sup>INFN Sezione di Ferrara and University of Ferrara, 44100 Ferrara, Italy

<sup>b</sup>INFN Laboratori Nazionali di Frascati, 00044 Frascati, Italy

<sup>c</sup>INFN Sezione di Roma1 - Gruppo Collegato Sanità and Italian National Institute of Health, 00153 Rome, Italy

<sup>d</sup>INFN Sezione di Genova, 16146 Genova, Italy

<sup>e</sup>INFN Sezione di Bari, 70126 Bari, Italy

<sup>f</sup>Thomas Jefferson National Accelerator Facility, Newport News, VA, 23606 USA

<sup>g</sup>Argonne National Laboratory, Lemont, IL, 60439 USA

<sup>h</sup>Duquesne University, Pittsburgh, PA, 15282 USA

<sup>i</sup>University of Connecticut, Storrs, CT, 06269 USA

<sup>j</sup>The George Washington University, Washington, DC, 20052 USA

<sup>k</sup>Universidad Técnica Federico Santa María, Casilla 110-V Valparaíso, Chile

## Abstract

A Ring Imaging Cherenkov detector has been installed in the CLAS12 spectrometer at Jefferson Laboratory (JLab) to provide kaon identification in the momentum range between 3 and 8 GeV. The detector adopts a hybrid optics solution with aerogel radiator, light planar and spherical mirrors, and highly segmented photon detectors. We report here on the design, construction, and initial performance of the RICH during the commissioning of the detector and the first physics data taking period.

**Keywords:** Ring-imaging Cherenkov detectors, PID detectors, Single-photon detection

## 1. Overview

Particle identification (PID) of hadrons in the original baseline design of the Forward Detector of CLAS12 is obtained by combining the information from the High Threshold Cherenkov Counter (HTCC) [1], Low Threshold Cherenkov Counter (LTCC) [2], and Forward Time-of-Flight (FTOF) [3] systems. However, no sufficient separation of kaons from pions and protons can be achieved by using only these detectors in the momentum range relevant for the approved semi-inclusive deep inelastic scattering (SIDIS) physics program, i.e. between 3 and 8 GeV. Therefore, improved particle identification in this momentum range is achieved by replacing two sectors of the existing LTCC with Ring Imaging Cherenkov (RICH) detectors. The first module of the RICH detector was completed before the start of the physics run, see Fig. 1, while the installation of the second module in the opposite sector is foreseen for the beginning of the CLAS12 operation with polarized targets. This article reports on the design, construction, and initial performance of the first RICH module. The second module will be identical to the first one.

The idea of a RICH detector is based on the fact that when a fast particle crosses a radiator with a velocity  $\beta$  larger than the velocity of the light in that medium, it generates Cherenkov radiation. The light is emitted in a cone with opening angle  $\theta_C$  given by  $\cos(\theta_C) = [\beta n(\lambda)]^{-1}$ , where  $n(\lambda)$  is the refractive index of the radiator, which may depend on

the wavelength  $\lambda$ . After a gap region where the cone opens up, the photons are detected and the ring can be reconstructed. A precision measurement of the Cherenkov angle provides the velocity of the particle and, together with information from the tracking system, it allows its identification. Thus, the capability of identify particles with a known momentum and different velocity is governed by the Cherenkov angle resolution, and it can be effectively parameterized by the separation in units of resolution  $n_\sigma$  between the angle distributions for the various particles.

## 2. The RICH Detector Requirements and Design

The CLAS12 spectrometer in Hall B [4] is designed to operate with highly polarized beams and nucleon targets at a luminosity of  $10^{35} \text{ cm}^{-2}\text{s}^{-1}$ . Under these conditions the production rate of protons, kaons, and pions studied using SIDIS Monte Carlo event-lists is such that, in most of the kinematic plane, the kaon rate is about one order of magnitude lower than the rate of pions and protons. Thus, successful kaon identification requires a rejection factor from pions around 1:500, i.e. a contamination in the kaon sample of a few percent. This corresponds to  $4\sigma$  separation. In the momentum range between 3 and 8 GeV, neither gas nor liquid radiators provide sufficient angular separation to achieve the required pion rejection factor (see Fig. 2) and the only viable solution is silica aerogel, an amorphous solid network of  $\text{SiO}_2$  nanocrystals



Figure 1: The first module of the CLAS12 RICH installed in Sector 4 of the Hall B Forward Carriage.

52 with a very low macroscopic density and a refractive index in  
53 between gases and liquids.

54 To detect the Cherenkov light emitted in the visible wave-  
55 length range, Hamamatsu Multi-Anode PhotoMultiplier Tubes  
56 (MaPMTs) were chosen for their high quantum efficiency  
57 in the visible and near ultraviolet (UV) regions, their fast  
58 response, and the required spatial resolution. Since the RICH  
59 detector must fit into the original CLAS12 Forward Carriage,  
60 there were several constraints imposed upon its design. Each  
61 sector required a projective geometry, limited depth of 1.2 m,  
62 and  $\sim 4.5 \text{ m}^2$  entrance windows. Simulation studies favored  
63 a hybrid imaging Cherenkov detector design incorporating  
64 aerogel radiators, visible light photon detectors, and a focusing  
65 mirror system. The focusing mirror system is used to reduce the  
66 detection area instrumented by the photon detectors to  $\sim 1 \text{ m}^2$   
67 per sector, minimizing costs and influence on the downstream  
68 FTOF and Electromagnetic Calorimeter [5] systems. Depending  
69 upon the incident particle track polar angle, Cherenkov  
70 light is either imaged directly or after one or more reflections  
71 and passes through the aerogel. Figure 3 shows a schematic  
72 view of two examples of direct imaging and imaging after  
73 multiple reflections. Such a peculiar hybrid-optics design is an  
74 innovative solution that has been successfully validated with a  
75 test-beam campaign [6].

76 The RICH detector replaces two sectors of the existing gas  
77 Low Threshold Cherenkov detector (LTCC), which is located at  
78 a 5-m distance from the beam-target interaction point. The first  
79 RICH module was designed while the CLAS12 spectrometer  
80 was already under construction and, as a consequence, it had to  
81 cover the same large area to match the trapezoidal shape of the  
82 LTCC sector. This resulted in several challenging requirements  
83 for the mechanical structure. The guiding principles were  
84 to minimize the material budget inside the acceptance and  
85 to limit the impact on the downstream detectors, ensuring at

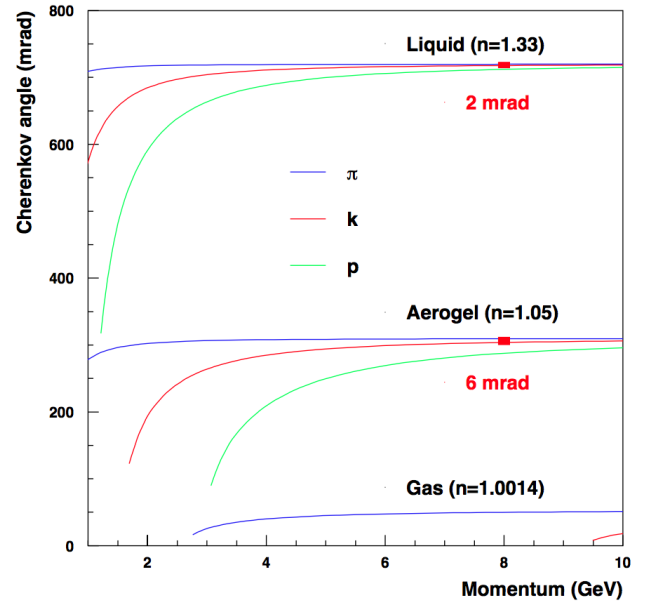


Figure 2: Cherenkov light opening angle as a function of the momentum for different particles using liquid, gas, or aerogel radiators. The angular separation between kaons and pions at the highest momenta is also indicated.

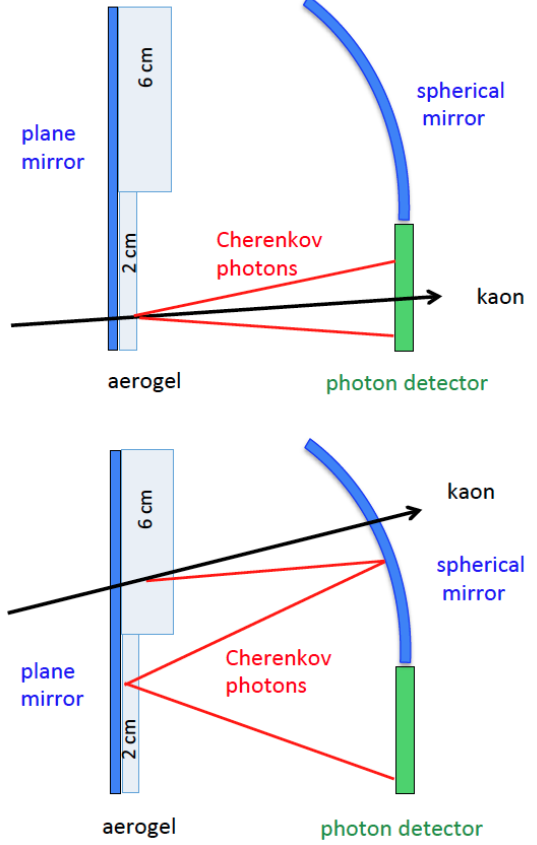


Figure 3: Examples of CLAS12 RICH imaging: direct detection of the Cherenkov cone produced in the thin aerogel layer (top plot); detection of the Cherenkov cone produced in the thick aerogel layer after multiple reflections and passes through the thin aerogel layer (bottom plot). The plot is not to scale.

the same time the rigidity of the structure imposed by the optical requirements. Therefore, light materials, in particular carbon fiber, were largely utilized for all elements inside the CLAS12 acceptance. For all the parts with large dimensions, the sandwich technique, in which two thin solid skins are glued together on a thick honeycomb core, was also used. This technique indeed combines high stiffness with substantial weight reduction, resulting in a total weight of the detector of about 900 kg, ~30% lower than the LTCC.

A sketch of the detector is shown in Fig. 4. It is composed of a trapezoidal box (larger base of 4.2 m, smaller base of 0.3 m, height of 3.7 m, and depth of 1.2 m) in which all of the active elements are installed: the wall of aerogel tiles, the mirrors, the photomultiplier tubes (PMTs), and the electronics. The main structural elements of the box are: the two lateral panels made of aluminum sandwich, the top panel made of carbon-fiber sandwich, and the two upper angular elements and the bottom element made of aluminum. Each of the lateral panels supports two planar mirrors, while another planar mirror is installed on the bottom of the box. The box is closed on the front face (with respect to the beam direction) by two entrance panels made of a sandwich of two 1-mm-thick carbon-fiber skins glued on a Nomex honeycomb core. Two planar mirrors with a wall of 2-cm-thick aerogel tiles are installed on the lower entrance panel, while a wall made of two layers of 3-cm-thick aerogel tiles is installed on the upper one. Therefore, the profile of the entrance panels was specifically designed not only to ensure the best light and gas tightness, but also to include stiffening ribs for the installation of the mirrors and the aerogel. The same sandwich structure was used for the electronics panel, located on the bottom part of the backward face of the box. It is composed of a main panel where all of the front-end electronics and the PMTs are installed, and a thin cover. The panel and the cover are screwed together on the mechanical structure, making a very rigid system. Finally, a very light exit panel made of a thin Tedlar sheet glued on an aluminum frame not supporting any active element, closes the back face of the trapezoidal box.<sup>143</sup>

The total material budget of the detector is largely dominated by the electronics panel, which contributes to approximately  $0.3X_0$  in the region from the beamline up to about  $17^\circ$ . A sizable contribution comes also from the aerogel (with a maximum contribution of  $0.05X_0$  in the polar angles from  $17^\circ$  to  $26^\circ$ ), while other active components like the spherical and planar mirrors contribute only  $\approx 0.01X_0$  each. The total material budget of the passive elements is estimated to be, on average, below  $0.05X_0$ .<sup>151</sup>

The mechanical structures and all of the active elements (mirrors, aerogel, electronics, MaPMTs) define the RICH detector. The RICH is attached to the CLAS12 Forward Carriage by means of steel connections, attached to the angular and bottom elements. Detailed Finite Element Analysis (FEA) studies were performed in order to optimize the design of the detector with respect to the maximum deformation allowed by the required accuracy of the optical systems. These studies included optimization of the ratio between the skin and honeycomb thicknesses of the sandwich, and of the total thickness and profile of various stiffening and connection elements.<sup>153</sup>

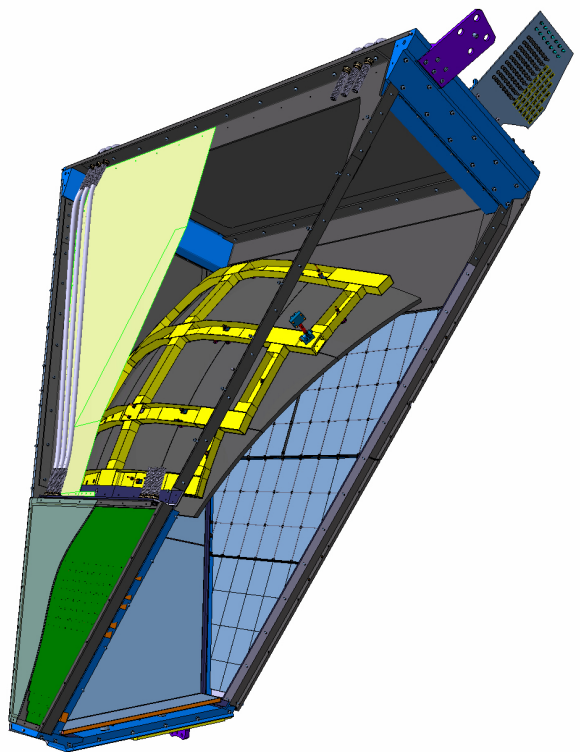


Figure 4: A schematic drawing of the CLAS12 RICH (rear view) with the internal components highlighted. From left to right, the components of the upper half are exit panel, spherical mirror support and sub-mirrors, double 3-cm-thick aerogel layer, and entrance panel. The components of the lower half are cover, electronics panel - mounting the front-end readout and the MaPMT sensors, 2-cm-thick aerogel layer, front planar mirrors, and entrance panel.

Simulations of the load conditions during the assembly and installation of the detector and in the RICH final position in CLAS12 were also performed together with a seismic analysis<sup>1</sup>. These simulations demonstrated that all stresses produced on the detector elements during the installation are well inside the elastic regime, and that the total deformations expected when the RICH is installed in CLAS12 never exceed a few mm.

### 3. The RICH Detector Components

#### 3.1. The Aerogel Radiator

The aerogel radiator was produced by the *Budker and Boreskov Institute of Nuclear Physics* (Russia), which was able to fabricate tiles of different shapes and thicknesses, a critical requirement of the complex CLAS12 geometry. A total of 102 tiles with nominal refractive index 1.05, cut into squares  $200 \times 200$  mm<sup>2</sup>, as well as pentagonal, trapezoidal, and triangular shapes, were assembled in two sections. The first section, covering the region between the beam pipe and the polar angle of  $17.5^\circ$ , was made of one layer of 2-cm-thick tiles.

<sup>1</sup> According to US regulations, seismic analyses are performed by increasing the expected weight load by 10%.

161 The second section, covering the polar angles between  $17.5^\circ$   
 162 and  $26^\circ$ , was made of two layers of 3-cm-thick tiles, the largest  
 163 aerogel tiles ever used in Cherenkov imaging applications at  
 164 this high value of refractive index.

165 Each tile was tested to determine the geometric and optical  
 166 parameters [7]. The measured geometric parameters are the  
 167 side length and thickness, and the planarity of the tile surface.  
 168 The measured optical parameters include the refractive index at  
 169 the reference wavelength of 400 nm, and the light transmission  
 170 as a function of the wavelength. The transparency parameter  
 171  $A_0$ , the clarity parameter  $C$ , and the scattering length  $L_{scatt}$  at  
 172 400 nm are then extracted from the measured optical properties  
 173 using the Hunt parameterization [8]. Distributions of the  
 174 measured values of the refractive index,  $A_0$  (in percent), and  
 175  $L_{scatt}$  for the square 2 cm tiles are shown in Fig. 5. The average  
 176 values obtained over all of the tiles are  $L_{scatt} = 50.5$  mm,  $A_0 =$   
 177  $0.975$ , and  $C = 0.00512 \mu\text{m}^4/\text{cm}$ . From these measurements,  
 178 the expected photon yield for  $\beta = 1$  particles is estimated to be  
 179 about 19 photoelectrons (p.e.) in the 2 cm sector and about 25  
 180 in the 6 cm (3 cm + 3 cm) sector.

### 181 3.2. The Mirror System

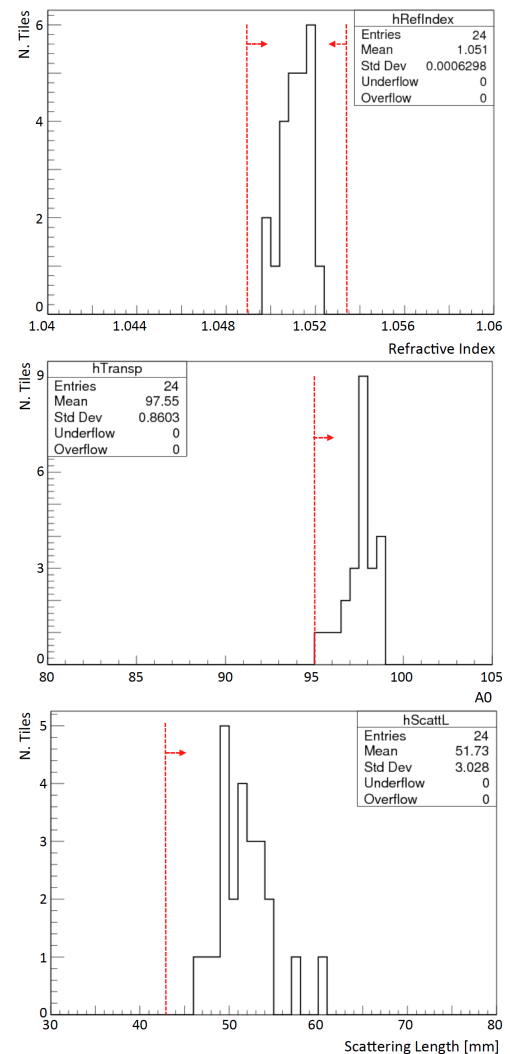
182 The mirror system, composed of planar and spherical mirrors,  
 183 was designed to minimize the photon loss and to direct  
 184 as much of the Cherenkov radiation as possible toward the  
 185 photodetectors. Simulations were performed to optimize the  
 186 segmentation, the position, and the radius of curvature of  
 187 these mirrors, and to define the specifications of the optical  
 188 performance. A drawing of the system is shown in Fig. 6.

#### 189 3.2.1. The Spherical Mirrors

190 The spherical mirror system, installed inside the RICH box  
 191 in front of the exit panel, has a total surface of about  $3.6 \text{ m}^2$ ,  
 192 a radius of curvature  $R = 2.7 \text{ m}$ , and is segmented into 10  
 193 sub-mirrors. They were produced by the *Composite Mirror*  
 194 *Applications* company [9], and are made of two layers of  
 195 carbon fiber glued on a honeycomb core of small carbon-fiber  
 196 cylinders. The areal weight of these mirrors is less than  
 197  $5 \text{ kg/m}^2$ , with an improvement of about 20% with respect  
 198 to the mirrors produced by the same company for the LHCb  
 199 experiment [10]. Each mirror is positioned on a light carbon  
 200 frame by means of three special joints equipped with a spring  
 201 and a precision screw that allowed their relative alignment. The  
 202 frame is then attached to the mechanical structure by means of  
 203 three similar joints that allow the alignment of the full mirror  
 204 system with respect to the other active elements of the detector.

205 The accuracy of the spherical surface of the sub-mirrors was  
 206 quantified by means of a so-called spot size measurement, in  
 207 which each mirror was illuminated with a point-like light source  
 208 and the size of the reflected spot was measured by a XIMEA  
 209 camera with a 1-cm-wide CMOS sensor. The size of the spot  
 210 is quantified by  $D_0$ , which is defined as the minimum diameter  
 211 containing 90% of the total reflected light, and is related to the  
 212 angular resolution of the reflected photons by the relation

$$213 \sigma_\theta = \frac{D_0}{8R}. \quad (1)$$



214 Figure 5: Distributions of the measured refractive index (top plot),  $A_0$  (in  
 215 percent, central plot), and  $L_{scatt}$  (bottom plot) for the square 2 cm tiles. The  
 216 red dashed lines indicate the specification limits.

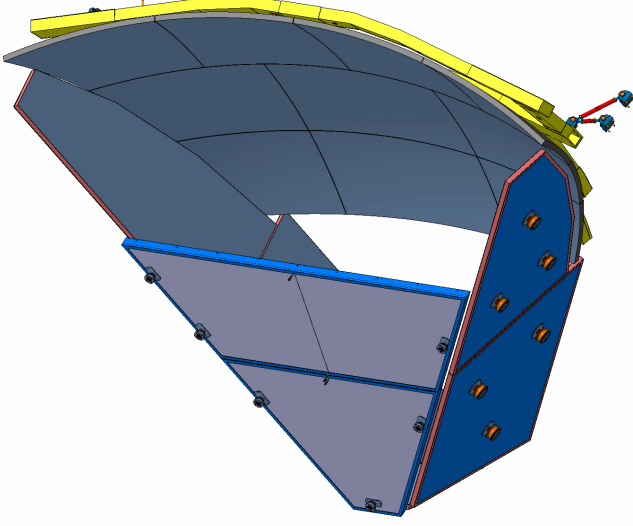


Figure 6: Drawing of the CLAS12 RICH mirror system with their mounting joints (front view). The 10 sub-mirrors of the spherical mirror face the two front planar mirrors. An array of planar mirrors, two on each side and one (not visible) on the bottom, completes the light-containment system.

213     The smaller  $D_0$  is, the closer the mirror surface is to a perfect  
 214     sphere. The measurements also allow for the extraction of the  
 215     radius of curvature, which corresponds to the distance between  
 216     the camera and the mirror where the spot size is minimal.  
 217     The results of a typical measurement of one sub-mirror are  
 218     shown in Fig. 7, where  $D_0$  as a function of the distance and  
 219     the shape of the spot at the beginning of the distance scan and  
 220     at the minimum are shown. All of the sub-mirrors exhibit a  
 221      $D_0$  smaller than 1.5 mm, which means  $\sigma_\theta$  significantly below  
 222     1 mrad, and a variation in the measured radii below 0.5%. All  
 223     of these numbers are well within the specifications.

224     The sub-mirrors were coated with a reflecting layer by  
 225     *Evaporated Coatings Inc* [11]. The quality of this coating was  
 226     verified by measuring the reflectivity on several surface spots  
 227     in the wavelength range from 300 to 650 nm. For all of the  
 228     sub-mirrors, we obtained on average a reflectivity between 88%  
 229     and 90%, relatively flat over the whole wavelength range.

### 230     3.2.2. The Planar Mirrors

231     The planar mirror system is composed of 7 mirrors: two  
 232     installed on each of the lateral panels, two on the front panel,  
 233     and one on the bottom, for a total surface area of about 6.5 m<sup>2</sup>.  
 234     These mirrors were produced by the *Media Lario* company [12]  
 235     and are made of two thin layers of glass glued on an aluminum  
 236     honeycomb core. This is a standard technique widely used in  
 237     telescopes for astrophysics studies but used for the first time  
 238     in nuclear physics experiments, and allows for the production  
 239     of mirrors as light as the carbon fiber ones but at much lower  
 240     cost. Being in the acceptance of the detector, the front mirrors  
 241     use very thin (0.7 mm) glass layers, allowing a reduction of the  
 242     material budget down to about 0.01X<sub>0</sub>, while for the lateral and  
 243     the bottom mirrors, thicker (1.6 mm) glass layers were used.

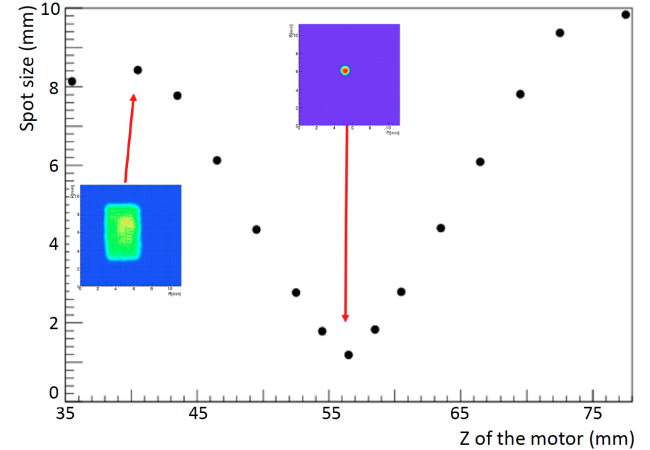


Figure 7:  $D_0$  as function of the distance between the mirror and the camera for one of the spherical sub-mirrors. The two inserts show the shape of the reflected spot at the beginning of the distance scan and at the minimum.

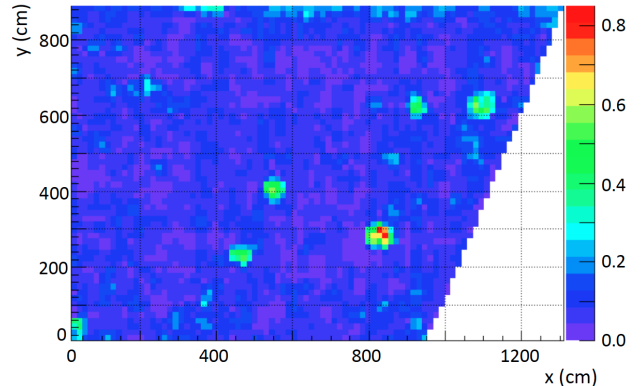


Figure 8: Profile of the local slope (indicated by the color scale in mrad) of the surface of one of the lateral planar mirror measured with a CMM.

The planarity of the mirror was measured with a Coordinate Measuring Machine (CMM). Typically, the measured accuracy of the surface was a few microns RMS. To better quantify the quality of the surface, the local slope profile was reconstructed from the spatial profile, as shown for one of the lateral mirrors in Fig. 8, where we see only a few spots with non-zero slope over a largely flat surface. All of the mirrors satisfy the requirement that only a few percent of the total surface should exceed a local slope of 0.3 mrad.

The characterization of the planar mirrors was completed by measuring the reflectivity in a few random spots of the surface in the wavelength range from 300 to 650 nm. The measurements showed a maximum reflectivity of approximately 95% at 400 nm and a reflectivity higher than 90% in the whole range.

### 3.3. The Photon Detector

Thanks to the use of mirrors, the active area is minimized to about 1 m<sup>2</sup>. The instrumented area is optimized to cover the most effective region close to the beam pipe, which is where the density of particles per unit area is the highest, the

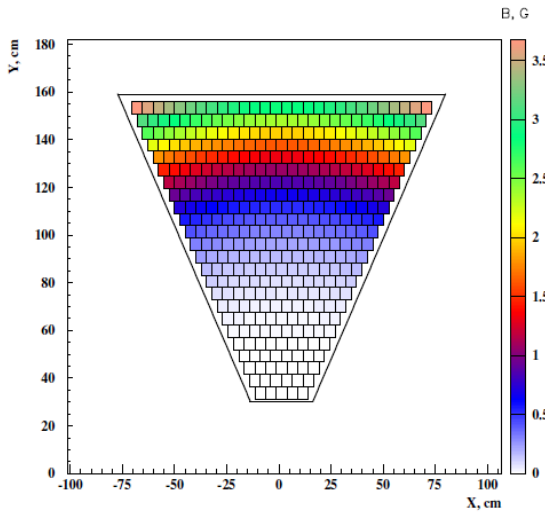


Figure 9: Calculated map of the torus fringe field strength (in Gauss) in the RICH photodetector area.

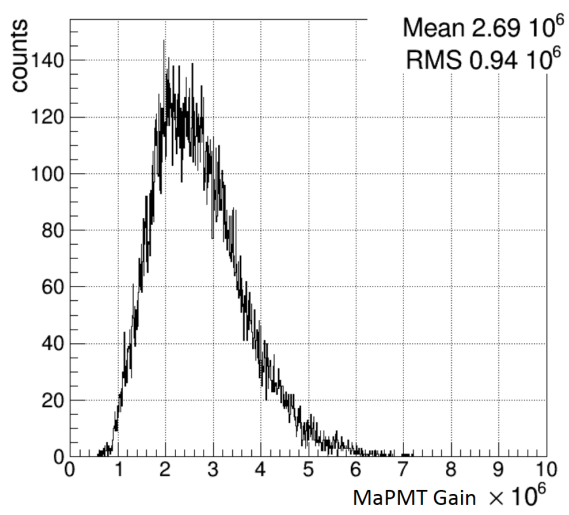


Figure 10: Distribution of the data-sheet gains of the 25k RICH MaPMT channels.

263 particle momenta are to a large extent above the FTOF working  
264 range, and the hadron identification requires the best RICH  
265 performance.

### 266 3.3.1. The Photosensor

267 Due to the imaging aspects of the RICH, there are several  
268 requirements that the photon sensor has to fulfill: it has to  
269 efficiently detect single photoelectron (SPE) level signals, it  
270 must be sensitive in the visible light wavelengths (due to the  
271 aerogel radiator material), it must have the spatial resolution  
272 required to achieve the design angular resolution, and it has to  
273 provide an active area with minimal dead space. In addition,  
274 it has to be insensitive to the low torus fringe field where the  
275 RICH readout is located, which is estimated to be no more  
276 than 3.5 G, see Fig. 9. The Hamamatsu flat-panel H8500<sup>299</sup>  
277 Multi-Anode PhotoMultiplier Tube (MaPMT) [13] with an<sup>299</sup>  
278 8×8 array of 6×6 mm<sup>2</sup> pixels over a compact active area of<sup>299</sup>  
279 5×5 cm<sup>2</sup> and with high packing fractions (89%), was initially<sup>300</sup>  
280 selected as a good candidate. Despite not advertised as the<sup>301</sup>  
281 optimal choice in the SPE regime, such MaPMTs showed<sup>302</sup>  
282 adequate performance in several laboratory tests [14] and beam<sup>303</sup>  
283 tests [15]. Just after the RICH construction startup, the novel<sup>304</sup>  
284 Hamamatsu H12700 became available, with the same layout as<sup>305</sup>  
285 the H8500, but an optimized dynode structure for single photon<sup>306</sup>  
286 detection [16].

287 Of the 391 MaPMTs that the CLAS12 RICH employs, 80<sup>308</sup>  
288 are of the H8500 type and the rest are of the H12700 type.<sup>309</sup>  
289 This results in a total of 25024 individual pixels, covering<sup>310</sup>  
290 the ~1 m<sup>2</sup> trapezoidal active area of the first RICH module.<sup>311</sup>  
291 The production specifications included requirements on the<sup>312</sup>  
292 minimum gain of  $1 \times 10^6$  and a maximum total dark current<sup>313</sup>  
293 of 5 nA. Both were fully achieved. Figure 10 shows the<sup>314</sup>  
294 distribution of the pixel gains, which has an average value of<sup>315</sup>  
295  $2.7 \times 10^6$ , corresponding to about 430 fC generated charge per<sup>316</sup>  
296 SPE.

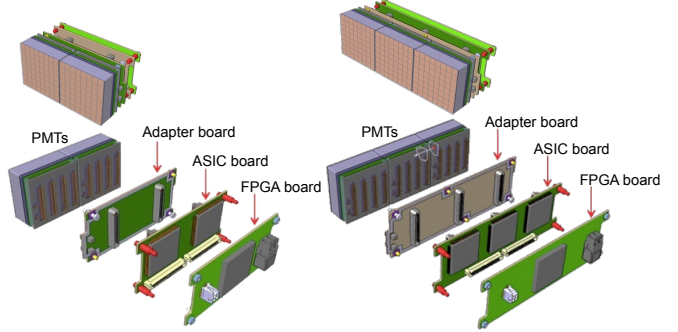


Figure 11: The CLAS12 RICH readout unit design (see text for details).

### 3.3.2. The Readout Electronics

The RICH front-end electronics are designed to ensure 100% efficiency at 1/3 of the average photoelectron signal level, 1 to 4 gain spread compensation, time resolution of the order of 1 ns to distinguish direct from reflected photon hits, and a trigger rate up to 20 kHz with 8  $\mu$ s trigger latency and negligible dead time [17].

The front-end electronics are organized into compact units (called tiles, see Fig. 11) mechanically designed to fit the MaPMT dimensions, each serving two or three MaPMTs, thus allowing the tessellation of large surfaces with minimum dead space and material budget. Each readout unit comprises three boards with complementary functions.

A feed-through adapter board provides the electrical connectivity of the sensors with the external readout system, while preserving the adequate light and gas tightness of the inner detector volume when mounted on the RICH carbon-fiber supporting panel. It also distributes the sensor bias voltage (with -1000 V as the nominal value).

The signal processing board is based on the MAROC3 chip [18], a 64-channel microcircuit dedicated to MaPMT

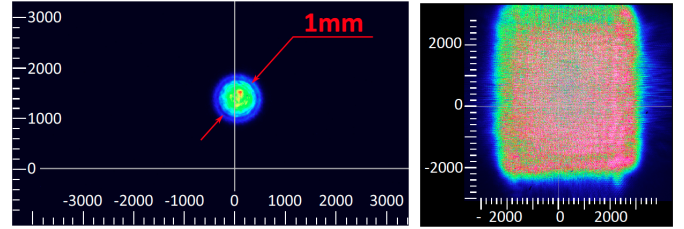
318 pulse processing. Each channel comprises a low impedance  
 319 adjustable gain preamplifier followed by two highly config-  
 320 urable shaping sections with independent processing. The first  
 321 section embeds a slow shaper and a sample-and-hold structure  
 322 to allow linear charge measurements up to 5 pC. Requiring  
 323 short trigger delays and multiplexed access, this section can  
 324 be used as a RICH calibration tool. The second section  
 325 features a fast shaper and an adjustable threshold discriminator  
 326 to produce, for each input signal, a start and stop logic pulse.  
 327 A constant-threshold binary readout requires good stability of  
 328 the baseline (pedestal) and definition of the working point (gain  
 329 and threshold). During the board production, quality assurance  
 330 tests confirmed the excellent sensitivity of the logic readout,  
 331 able to discriminate signals down to a few percent of a single  
 332 photoelectron discharge, as will be extensively discussed in  
 333 Section 4.2.

334 The third stage of the readout is made of the FPGA boards,  
 335 hosting a Xilinx7 FPGA chip, responsible for configuring and  
 336 reading the front-end MAROC3, distributing the trigger, and  
 337 interfacing with the data acquisition system [19] via optical  
 338 link. The FPGA provides a TDC functionality with a 1 ns  
 339 time stamp for both start and stop times. The start time is used  
 340 for timing purposes, while the difference between the stop and  
 341 start times, the so-called Time-Over-Threshold (ToT), provides  
 342 a non-linear estimate of the amplitude of the input signal and is  
 343 used for the time-walk correction, see Section 5.2. Finally, the  
 344 FPGAs also embed a scaler readout that is used as a calibration  
 345 and monitoring tool.

### 346 3.3.3. *MaPMT Characterization*

347 The characterization of hundreds of MaPMTs is a chal-  
 348 lenging problem. In order to test them efficiently within  
 349 a reasonable time frame, a fully automated test stand was<sup>374</sup>  
 350 built to evaluate 6 MaPMTs at once. The test stand consists<sup>375</sup>  
 351 of a 470 nm diode laser system, 2 long-travel motorized<sup>376</sup>  
 352 stands to drive a laser fiber in two-dimensional space for<sup>377</sup>  
 353 individual pixel illumination, and a motorized neutral-density<sup>378</sup>  
 354 filter system. The laser light is directed through the fiber<sup>379</sup>  
 355 and attenuated to the single-photon level using neutral-density<sup>380</sup>  
 356 filters to mimic the conditions of the RICH detector. The motors<sup>381</sup>  
 357 are remotely controlled to move the focused laser 1 mm beam<sup>382</sup>  
 358 spot across the entire surface of the MaPMT entrance window<sup>383</sup>  
 359 and illuminate one by one the 64 pixels individually (see<sup>384</sup>  
 360 Fig. 12a). Alternatively, one can illuminate the whole surface of<sup>385</sup>  
 361 the MaPMT photocathode at once using an Engineered Diffuser<sup>386</sup>  
 362 to produce a square pattern with a non-Gaussian intensity<sup>387</sup>  
 363 distribution (see Fig. 12b). The latter configuration was used for<sup>388</sup>  
 364 the massive characterization of the RICH MaPMTs, bringing<sup>389</sup>  
 365 routine workloads to a minimum. The evaluation of 6 MaPMTs<sup>390</sup>  
 366 (corresponding to 384 individual channels) at 4 different high<sup>391</sup>  
 367 voltages and 6 different light intensities was completed in 6<sup>392</sup>  
 368 hours with less than 15 minutes of human intervention. <sup>393</sup>

369 The characteristics of the SPE spectrum were studied using<sup>394</sup>  
 370 the charge measurement functionality of the slow shaper of<sup>395</sup>  
 371 the MAROC3 chip. A new computational model [20] for the<sup>396</sup>  
 372 description of the PMT response functions of both the H8500<sup>397</sup>  
 373 and H12700 MaPMTs was developed. Important features of<sup>398</sup>



(a) Focused laser beam.

(b) Square pattern.

Figure 12: The MaPMT test stand laser output options. The images are taken at an arbitrary distance from the source, the scale is in micron.

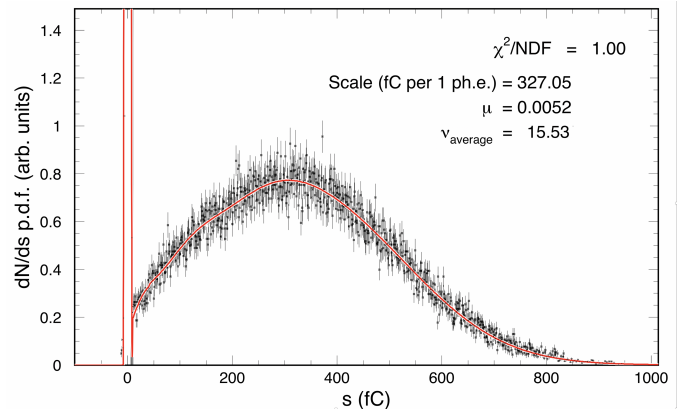


Figure 13: Sampled H8500 MaPMT single photoelectron spectrum from one of the pixels at 1000 V with a low-intensity laser light source. The fit function (see details in Ref. [20]) is shown as a solid line. The relevant parameters (see text) are  $\mu = 0.0052$ ,  $v_{average} = 15.53$ , and  $scale = 327$  fC. This corresponds to a MaPMT gain of  $2.0 \times 10^6$ .

the model include the ability to approximate the true SPE spectra from different PMTs with a variety of parameterized spectral shapes. The predictive power of the model was tested by demonstrating that the SPE spectral parameters, obtained in the measurements, well describe the amplitude distributions of the same photodetector measured at different levels of illumination. Thus, the model allowed us to extract the characteristic parameters of the devices independently of the test measurement conditions.

The SPE spectrum is extracted by fitting the signal amplitude distribution with the model function measured as shown in Fig. 13 for the H8500 MaPMT and in Fig. 14 for the H12700. The  $x$ -axis is calibrated in terms of charge measured by the MAROC3 chip. To approximate the performance of the first amplification cascade of the MaPMTs, the probability function was introduced in the model as a trinomial sum of three Poissonians with different average secondary multiplicities and the corresponding three relative probabilities for every photo-electron to generate secondary electrons (see Ref. [20] for more details). In each fit, the parameter  $\mu$  corresponds to the average number of photoelectrons generated at the photocathode by each laser pulse,  $v_{average}$  is the average number of secondary electrons generated at the first dynode, and  $scale$  is the average anode charge collected from one photoelectron.

In the single-photoelectron amplitude spectra shown in

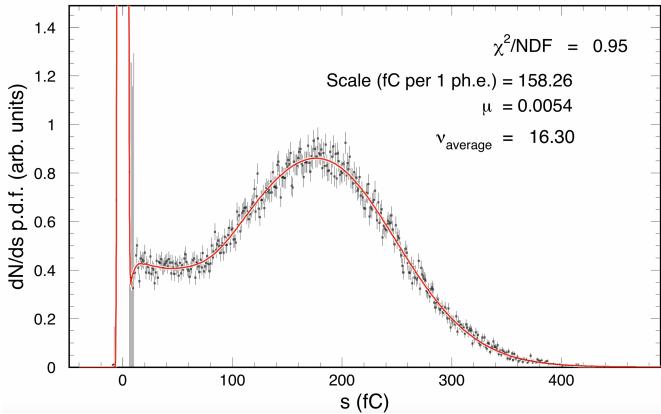


Figure 14: Sampled H12700 MaPMT single photoelectron spectrum from one of the pixels at 1000 V with a low-intensity laser light source. The fit function (see details in Ref. [20]) is shown as a solid line. The relevant parameters (see text) are  $\mu = 0.0054$ ,  $v_{\text{average}} = 16.3$ , and  $\text{scale} = 158.26$  fC. This corresponds to a MaPMT gain of  $0.98 \times 10^6$ .

399 Figs. 13 and 14, the normally significant contributions of the  
400 cross-talk signals, caused by the photoelectron amplification  
401 cascades in the neighboring PMT channels, have been removed  
402 by using the filter masks covering the neighbors, and leaving  
403 open only the pixel studied. The detailed discussion of the  
404 method will be given in [21]. The data showed that the H12700  
405 has, on average, a 10% better efficiency than the H8500, likely  
406 due to the improved photocathode performance and collection  
407 efficiency. An example of the results for one MaPMT is shown  
408 in Fig. 15. The parameter *scale* (top plot), characterizing  
409 the amplification (dynode) system, is virtually independent of  
410 the light radiation level, while strongly dependent on the high  
411 voltage setting, the exact behavior one would expect from the  
412 characteristics of the internal dynode system of a MaPMT.  
413 The central plot shows the average number of photoelectrons  
414  $\mu$  measured with different optical filters. It indicates that all  
415 of the channels respond in the same way as the light intensity  
416 increases. This parameter is practically independent of the  
417 applied voltage, as expected. The parameter  $v_{\text{average}}$  (bottom plot)  
418 that is related to the first dynode performance, has a weak  
419 dependence on the bias voltage and is independent of the level  
420 of light radiation as well.

421 The results of the characterization have been stored in the  
422 CLAS calibration database and are available for use in the  
423 Monte Carlo simulations. The extracted gain values have been  
424 used to perform the equalization of all 25024 readout channels.

425 The SPE spectra allow for the study of the SPE response  
426 dependence on the working parameters, i.e. MaPMT bias  
427 voltage, MAROC pre-amplification gain, and discriminator  
428 threshold <sup>2</sup> using the binary readout line. Data indicated that  
429 the efficiency reaches a plateau over a wide range of working  
430 parameter values [17]. The plateau corresponds to the region  
431 where all of the MaPMT discharges are digitized and the  
432 efficiency ultimately depends on the quality of the

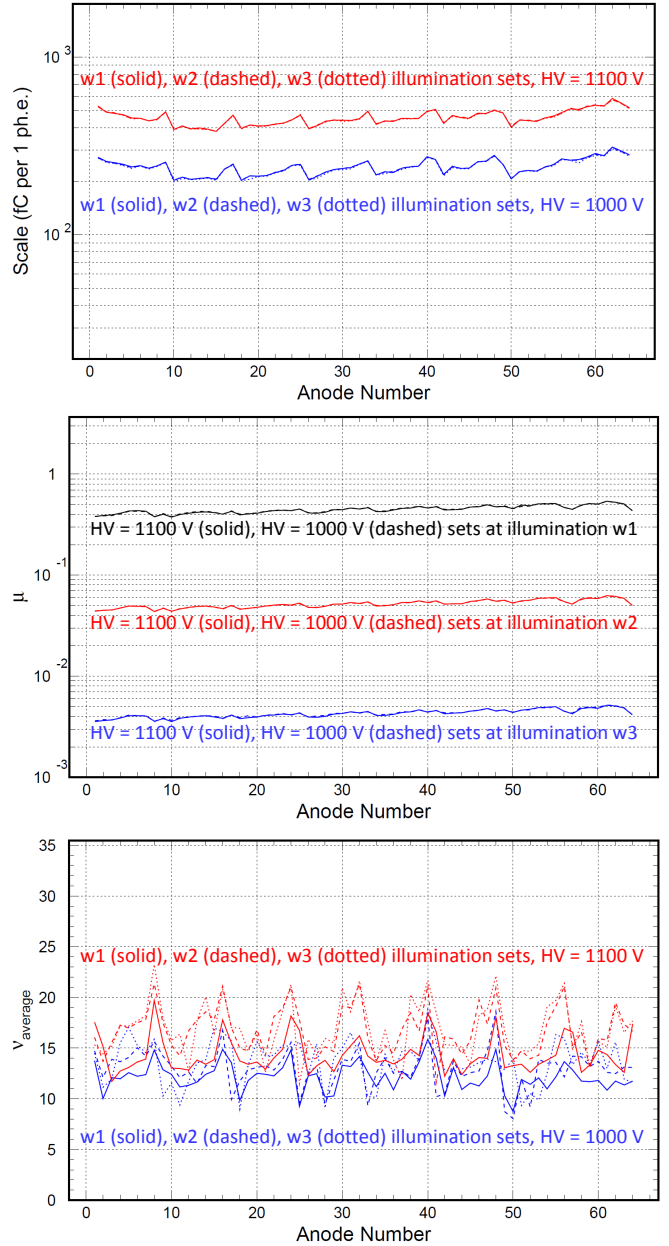


Figure 15: Distributions of fit parameters measured at 2 different high voltages (1000 V and 1100 V) and 3 different light intensities ( $w_1:w_2:w_3 \sim 100:10:1$ ) for 64 pixels of one MaPMT: the parameter *scale* characterizing the dynode amplification system (top), the average number of photoelectrons  $\mu$  (center), and the first dynode amplification  $v$  (bottom).

<sup>2</sup>The programmed threshold levels are expressed in Digital-to-Analog Converter (DAC) units, 1 DAC unit corresponds to about 1 mV.

433 photocathode. The plateau is a consequence of the saturated  
 434 mode employed in the MAROC binary readout and allows a  
 435 flexible definition of the working point, a crucial feature when  
 436 dealing with a large number of channels in the challenging  
 437 single-photon regime.

### 438 3.4. The Detector Services

439 The CLAS12 RICH requires various services, namely power,  
 440 cooling, and gas purge whose number of lines has to be  
 441 minimized and installed outside of the CLAS12 acceptance.  
 442 A continuous nitrogen flow, supplied by the Hall B gas  
 443 distribution system, is provided in order to keep the relative  
 444 humidity inside the RICH vessel at the few percent level. The  
 445 flow is set to about 40 l/m to ensure a complete inner volume  
 446 exchange every few hours. A backup system has been realized  
 447 by a stack of nitrogen bottles to allow for up to 3 days of gas  
 448 flow in case of failure of the primary distribution system.

449 The electronics power is controlled by a CAEN SY4527  
 450 power supply with five 8-channel A2518 low voltage (LV)  
 451 boards and five 32-channel A1536 high voltage (HV) boards.  
 452 Each LV channel powers 4 readout units, while each HV<sup>486</sup>  
 453 channel drives the MaPMTs grouped in one readout unit. The<sup>487</sup>  
 454 electronics readout is connected to the back-end by three MTP<sup>488</sup>  
 455 trunks of 2.5 Gbps optical fibers. One trunk groups several<sup>489</sup>  
 456 multi-core fibers, each of them connecting one of the eight ports<sup>490</sup>  
 457 in the VME/SSP [19] back-end module to four FPGA boards.<sup>491</sup>

458 The readout electronics dissipates about 3.5 W per unit,  
 459 mainly due to the FPGA chip and the optical transceiver, as  
 460 shown by the thermocamera image in Fig. 16. The total  
 461 heat load, at the level of 500 W, is removed by a forced air  
 462 flow. Since the electronics panel is not fully sealed due to the  
 463 numerous holes for the readout and HV connectors, there is a  
 464 diffusive exchange in the RICH vessel between the nitrogen gas  
 465 used to keep the aerogel dry and the air in the electronics panel.  
 466 As a consequence, dry and clean air is required to cool down the  
 467 electronics. This is achieved with an Altas Copco multi-core<sup>500</sup>  
 468 oil-free rotary scroll air compressor. The compressor fills a  
 469 tank at 8 atm pressure, from where the cooling air is filtered<sup>501</sup>  
 470 and circulated toward two distributors located at the sides of the  
 471 electronics panel and outside the acceptance. These are made<sup>502</sup>  
 472 of stainless-steel tubes with several nozzles to direct the cooling<sup>503</sup>  
 473 air supersonic flow along the board surface. The exhaust is<sup>504</sup>  
 474 made of six corrugated tubes that run in the back of the RICH<sup>505</sup>  
 475 module behind the spherical mirror.<sup>506</sup>

## 476 4. The RICH Detector Installation and Commissioning

### 477 4.1. RICH Assembly

478 The assembly of the RICH detector was performed in a clean<sup>515</sup>  
 479 room and each element was installed after the completion of the<sup>516</sup>  
 480 relative characterization tests. The trapezoidal RICH vessel was<sup>517</sup>  
 481 attached to a large aluminum structure with a pivot to rotate the<sup>518</sup>  
 482 detector from the vertical to the horizontal position, as required<sup>519</sup>  
 483 by the various assembly phases.<sup>520</sup>

484 The ten spherical sub-mirrors were mounted on a common<sup>521</sup>  
 485 frame inside the RICH vessel. To minimize the material budget,<sup>522</sup>

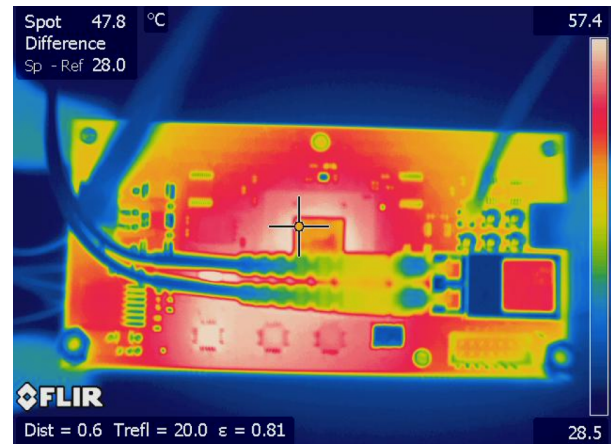


Figure 16: The CLAS12 RICH readout unit as imaged by a thermocamera. The hottest spots are the FPGA chip in the center and the optical transceiver on the right.

the frame is composed by a net of 1.5-mm-thick carbon-fiber U-profiles. Each element (frame and sub-mirrors) has three mounting points designed to allow precise alignment. The relative alignment of the sub-mirrors was performed with the same setup used to determine their surface accuracy. The full spherical mirror was illuminated by a point-like source and the position of each sub-mirror was adjusted until the ten spot images converged into the nominal center of curvature. In Fig. 17, the reflected images before the alignment (when each sub-mirror produces a spot at a different location) and after the alignment (when all the spots overlap within a few mm) are shown. The quality of the result is also visible in Fig. 18, where the spherical mirror system before (left) and after (right) the alignment is shown.

The lateral and bottom planar mirrors were attached to the RICH trapezoidal vessel structure by means of joints that allow for a precise alignment. The two front mirrors were mounted on the lower front panel made of carbon fiber. The relative position of the mirrors was aligned with respect to the RICH vessel at the level of about 0.5 mrad by using a faro-arm. The fully installed mirror system as seen from the entrance panel is shown in Fig. 19.

The RICH photon detectors and readout electronics were installed on the electronics panel using an independent aluminum support structure to enable easy access and to allow rotations during the functionality tests. The PMTs with higher gain were placed closer to the beam pipe, where better detection performance is required. As the MaPMT in one readout unit share the same HV bias, they were selected to be of similar gain and of the same type (H8500 or H12700). The fully equipped electronics panel is shown in Fig. 20 from the MaPMT side and in Fig. 21 from the readout electronics side.

After the electronics panel assembly was completed, particular care was devoted to minimize and stabilize the pedestal width values. The measured pedestal RMS was initially at the level of few DAC units, with relatively large variations not only from MaPMT to MaPMT but also among the channels of a

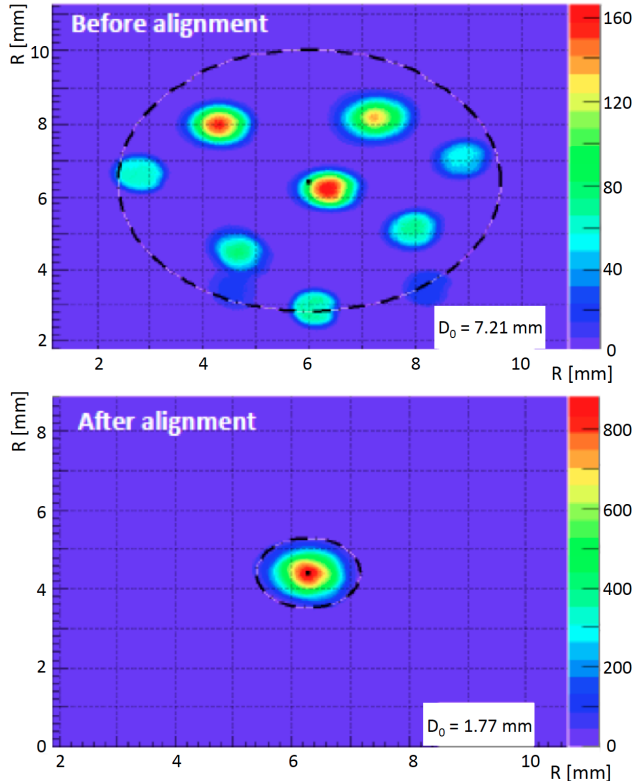


Figure 17: Reflected spot by the whole spherical mirror system: before the alignment (top plot), all sub-mirrors image the light source in different locations; after the alignment (bottom plot), all images overlap in the same position. The spot brightness depends on how close the sub-mirror center is to the sensor position.



Figure 18: The spherical mirror before (top plot) and after (bottom plot) alignment. As a result of the alignment, the image appears continuous along the whole mirror surface.

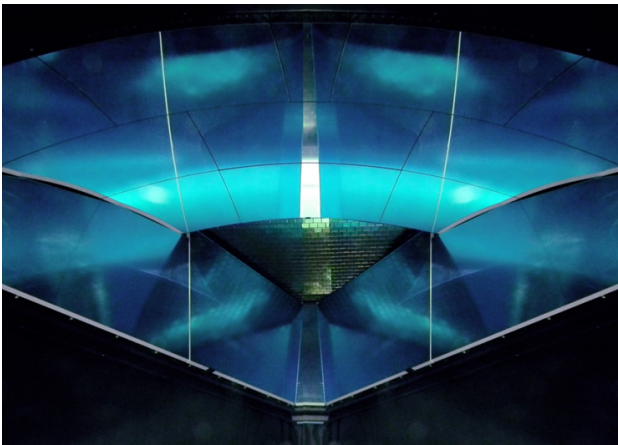


Figure 19: The mirror system as it is seen from the RICH entrance panel. Clockwise from the top, the ten spherical sub-mirrors, the two right lateral mirrors, the bottom mirror, and the two left lateral mirrors are visible. At the center, the MaPMT array is also visible.

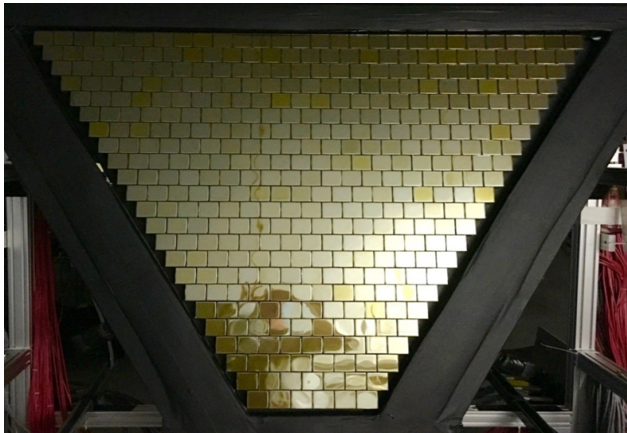


Figure 20: The fully assembled plane of MaPMTs.



Figure 21: The fully assembled and cabled front-end electronics. Visible are the gray 20 AWG LV cables, the red HTC-50-1-1 HV cables, and the cyan MTP<sup>540</sup> optical fibers.

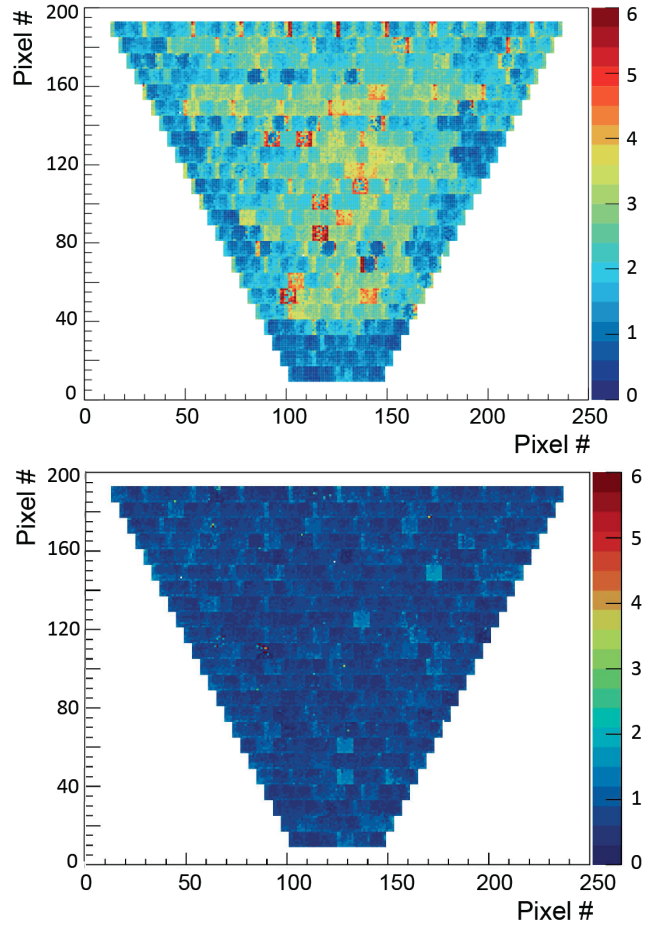


Figure 22: Map of the pedestal RMS values before (top) and after (bottom) the realization of a grounding grid connecting all of the electronics units to the RICH chassis to provide a common ground reference for the floating power lines.

single MaPMT, as shown in the top plot of Fig. 22. As the readout uses a single threshold value per chip (or MaPMT), the channel-by-channel variation may effect the single channel efficiency in a way that would be complicated to correct for. Therefore, a grounding grid was realized by connecting all of the boards to the detector chassis with a copper wire. In this way, all of the components of the readout system, powered by the floating 5 V low-voltage lines, were properly referred to the same ground. This reduced the typical pedestal RMS down to about 1 DAC unit, a level comparable with the test bench results, as shown in the bottom plot of Fig. 22.

Several tests were performed using cosmic rays at various stages of the electronics assembly. In the absence of a precise measure of the cosmic particle momentum, it was not possible to perform any study of the Cherenkov angle resolution. Nevertheless, cosmic runs allowed for the validation of the translation tables relating the electronics channels to the pixel positions, the development of the ring reconstruction software, the verification of the stability of the system, and the testing of the performance of the power supplies, cooling, readout, slow controls, and interlock services. After all planned tests

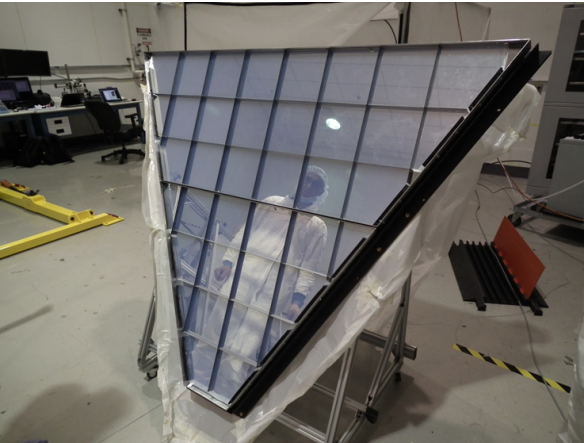


Figure 23: The 2-cm-thick section of the aerogel mounted on the two RICH front mirrors. Visible are the external aluminum frame and the black foam net that optically and mechanically isolates each tile from the others.

544 were completed, the complete readout system was eventually  
545 transferred into the mechanical structure.

546 The aerogel was the last element installed, being the most  
547 sensitive to the external conditions. For this reason, before  
548 its assembly, a test to verify the gas-tightness of the RICH  
549 vessel, temporarily completed with all of the closing panels,  
550 was performed. Each aerogel tile was inspected and mounted  
551 in a pre-selected location of the supporting structure, namely  
552 the front mirrors for the 2-cm tiles and the upper front panel  
553 for the 3-cm tiles. The location of each tile was determined in  
554 order to concentrate the tiles with the higher expected photon  
555 yield at forward polar angles where the particle identification  
556 requirements are most demanding. In addition, tiles with close  
557 optical properties were coupled in the same location of the  
558 double 3-cm layer. The tiles were secured in place by a net  
559 of nylon wires that ran along the edges and, on the side, by  
560 plastic bumpers covered by a thin foam layer to avoid damage  
561 to the aerogel. The tiles were also optically isolated from each  
562 other by using a thin layer of foam stretched around each tile.  
563 In fact, photons produced in one tile and propagating through  
564 an adjacent tile undergo surface effects that generally degrade  
565 the angular resolution. The foam is instrumental to avoid sharp  
566 edge contacts between the blocks that might originate cracks in  
567 the aerogel material. In addition, the foam net bonds the tiles  
568 together in forming a sole and stable layer. Figure 23 shows the  
569 front planar mirror system with the aerogel tiles fully installed.  
570

571 During the assembly, the aerogel panels were maintained in  
572 a low-humidity atmosphere (around 20% relative humidity) to  
573 prevent moisture absorption. Once the assembly of all tiles  
574 was completed, the panels were quickly installed on the RICH  
575 vessel, the detector was sealed with all of the closing panels and  
576 a flow of purged nitrogen was started to minimize the exposure  
577 to the external environment conditions.

578 Once the detector was sealed and before the transportation to  
579 the experimental hall, its functional parameters were tested for  
580 several weeks in the assembly room. The tests included the two  
581 gas systems serving the RICH: the nitrogen system that must  
582

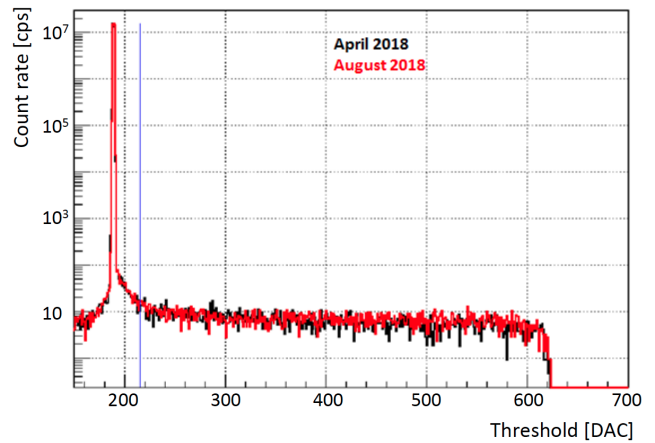


Figure 24: Example of a SPE spectrum from the dark rate measurement of one readout channel as a function of the threshold value. The two histograms were recorded in April and August 2018. The blue line indicates the threshold setting.

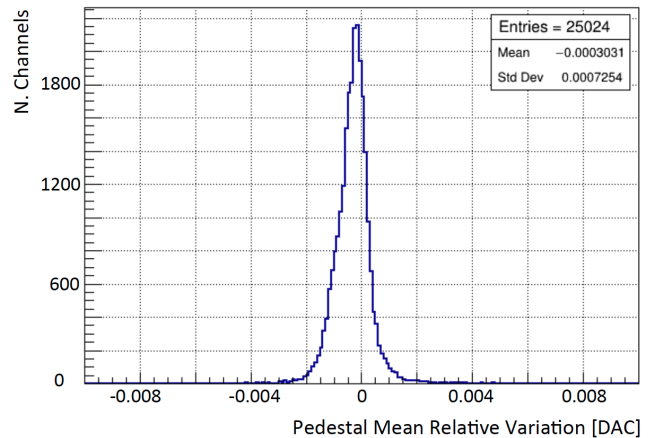


Figure 25: Relative variation of the mean pedestal position of the 25024 readout channels between April and August 2018.

keep the internal humidity at the few percent level to preserve the aerogel optical performance and the air-cooling system of the readout electronics.

#### 4.2. RICH Commissioning

The RICH detector was installed in the CLAS12 spectrometer at the beginning of January 2018, in time with the start of the first data taking in Hall B. In preparation for the data taking, a number of tests were routinely performed without and with beam to establish the running conditions and to verify the stability of the response.

The basic tool to monitor the RICH front-end electronics is provided by the measurement of the MaPMT dark noise counting rate. The number of counts above a programmed threshold is recorded for a time on the order of a second. A fine scan of the threshold value allows for the reconstruction of the full SPE spectrum for each of the 25k channels. An example of one SPE spectrum is shown in Fig. 24. The main

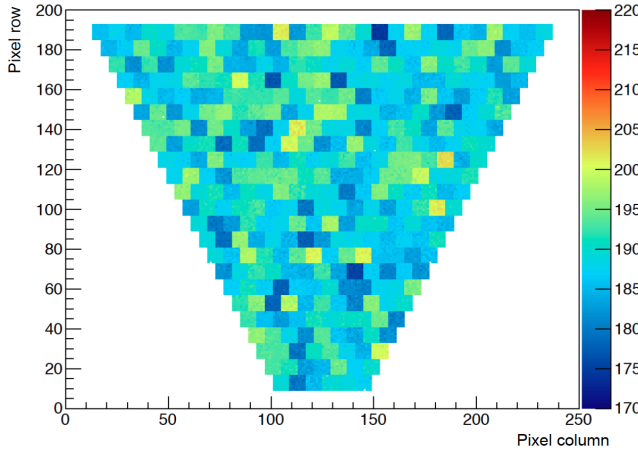


Figure 26: Map of the mean pedestal position in DAC units (color scale).

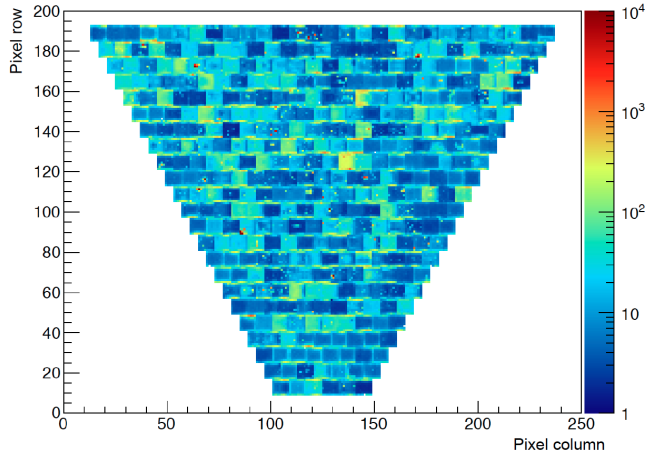


Figure 27: Map of the average dark count rate in the plateau region of threshold values (color scale).

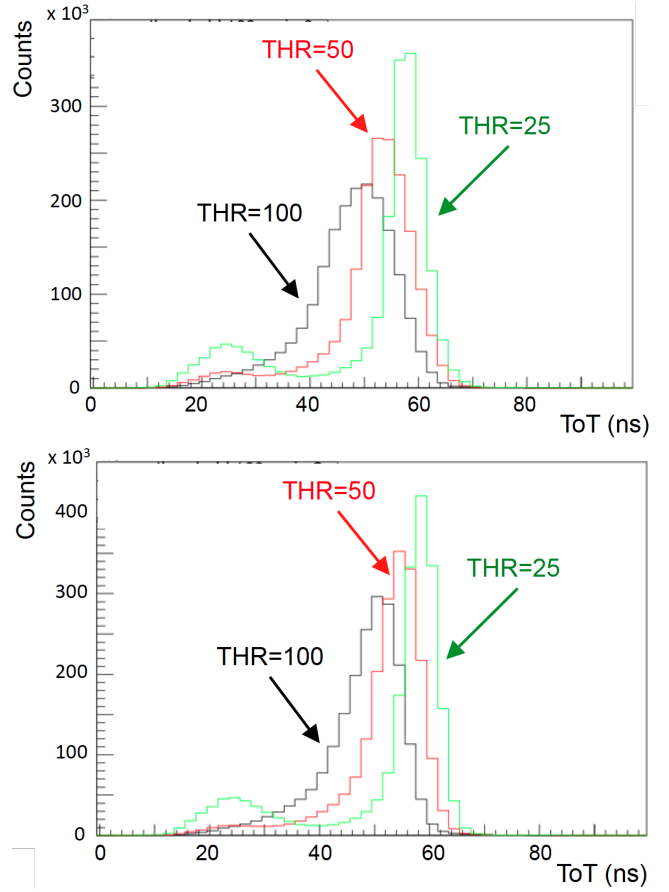


Figure 28: Time-over-Threshold (ToT) distributions of the RICH channels at three typical values of threshold (25, 50, and 100 DAC) without (top) and with (bottom) gain equalization. The saturated SPE signals generally yield ToT durations greater than 40 ns. When lowering the threshold weaker cross-talk signals are also recorded with ToT durations around 25 ns. Figure taken from Ref. [17].

598 features of the data are: *a*) a very narrow pedestal where the threshold equals the analog baseline, *b*) a region close to the pedestal where the rate smoothly decreases as the threshold increases (corresponding to the almost linear regime of the MAROC), and *c*) a large plateau of the saturation regime, where the count rate is basically insensitive to the threshold setting almost up to the edge of the SPE region. The plateau is a crucial feature of the front-end electronics, because it allows a flexible definition of the working point without the need for extreme precision in the channel equalization. Counts at threshold values below the pedestal are due to the bipolar shaped signal. The spectra allow for the channel-by-channel extraction of the pedestal position and width, the dark count rate in the plateau region, and the amplitude of the SPE region. The black and red histograms in Fig. 24, taken in April and August 2018, respectively, demonstrate the stability of the readout system over several months of running. Moreover, in Fig. 25, the relative variation of the mean pedestal position in the same interval of time is shown. On average, the pedestals are stable at the level of  $10^{-3}$ .

600  
601  
602  
603  
604  
605  
606  
607  
608  
609  
610  
611  
612  
613  
614  
615  
616  
617  
618

The pedestal level is different for each readout channel, but it is quite uniform within one MAROC chip, as can be seen from the map shown in Fig. 26. This result guarantees the effectiveness of the common threshold.

The average count rate in the plateau region provides a measurement of the dark count rate of the channel, as shown in the map of Fig. 27. The typical dark count rate is a few tens of Hz, with more than 99% of the channels below 100 Hz and only few channels above 10 kHz. It is also found that the highest dark count rates in the MaPMTs are located in the first and last row of pixels. Although measured with a completely different setup, these results are in good agreement with the values quoted in the Hamamatsu data sheets.

The MAROC preamplifier equalization gains are determined using the characterization measurements described in Section 3.3.3 by tuning the average MaPMT+MAROC gain to  $2.7 \times 10^6$  in all channels. The equalization gains range from about 0.5 to 3, with an average value of 1.2. The effect of the channel-by-channel signal equalization was verified during the engineering run by taking data at various thresholds for different MAROC gain configurations. Figure 28 shows the

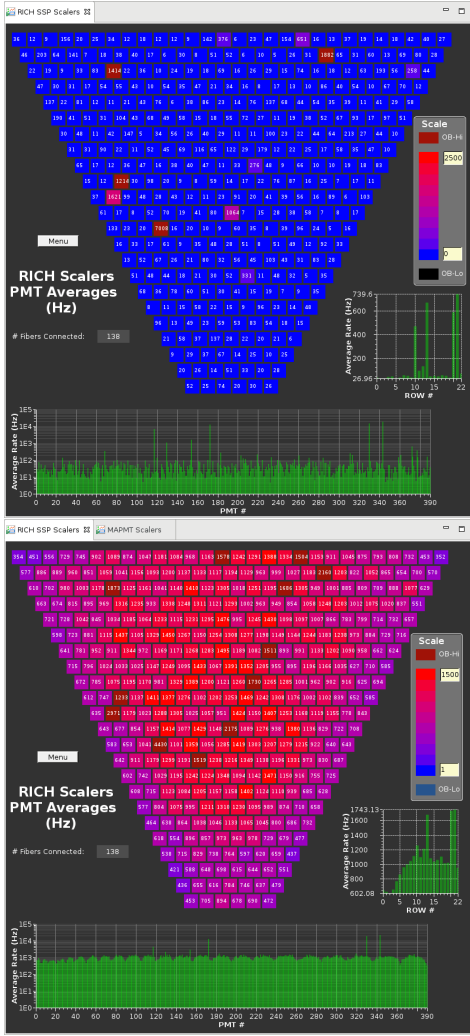


Figure 29: The average count rates (in Hz) over 64 pixels for each MaPMT<sub>670</sub> during data taking. Top: without beam on target, Bottom: with beam.

639 ToT distribution for three typical values of the threshold,  
 640 on the top for all channels without amplification (nominal  
 641 MAROC gain of 1) and on the bottom after equalization. After  
 642 equalization, the ToT distribution of saturated SPE signals is  
 643 narrower than with unitary gains. With typical ToT values  
 644 larger than 40 ns, the signal region is also clearly separated from  
 645 the cross-talk signals whose ToT values are distributed around  
 646 25 ns.

647 After these tests, the common discriminator thresholds were  
 648 set to +25 DAC units above the average MaPMT pedestal  
 649 position, a level that corresponds to a small fraction of the  
 650 average SPE amplitude.

#### 651 4.3. RICH Slow Controls and Interlocks

652 The RICH slow controls are based on Experimental Physics  
 653 Industrial Control System (EPICS) [22]. It includes EPICS  
 654 input-output controllers (IOCs) interfacing with different types  
 655 of hardware via communication protocols and over 25k RICH  
 656 process variables (PVs). The controls system monitors many<sub>689</sub>

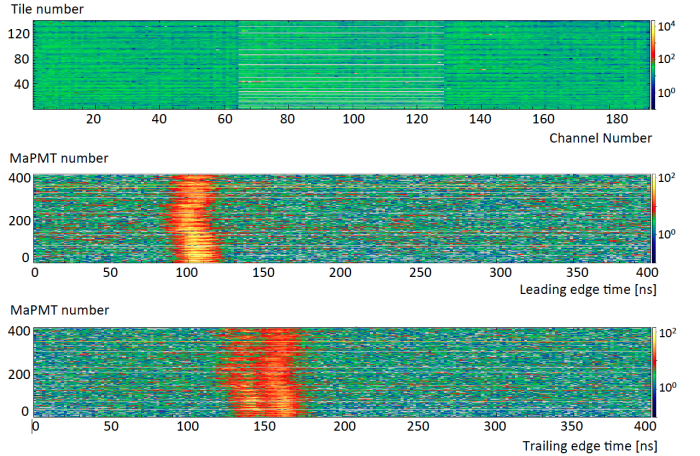


Figure 30: Online monitor plots of the TDC occupancy with beam on. From top to bottom: channel occupancy in terms of the tile vs. channel number; leading edge time distributions per MaPMT; trailing edge time distribution per MaPMT.

557 aspects of the RICH detector, such as the scaler rates of all 25k  
 558 Hamamatsu MaPMT pixels, the FPGA temperatures of each  
 559 readout board, the HV and LV power supplies, the LV and  
 560 current consumption of each readout unit, the gas system, and  
 561 the temperature and humidity of the electronics panel volume  
 562 and detector volume. For the Graphical User Interface (GUI),  
 563 the Control Systems Studio (CS-Studio), an Eclipse-based suite  
 564 of tools for developing and monitoring large-scale control  
 565 systems, is used.

566 The quality of the data is monitored by scaler and TDC  
 567 plots. Figure 29 shows the average MaPMT rate measured by  
 568 the scaler readout system when the beam is off (top plot)  
 569 and when the beam is on (bottom plot). In the top plot, the few  
 570 MaPMTs with hot pixels where the dark rate is substantially  
 571 higher than the average can easily be seen. The bottom plot  
 572 shows that when the beam is on the rate is always dominated by  
 573 physics events. Figure 30 shows the occupancy plots from the  
 574 TDC readout. The top plot shows the occupancy per channel,  
 575 and the center and bottom plots show the distributions of the  
 576 leading and trailing edge times per MaPMT, respectively. All  
 577 of these plots are used during the data taking to identify possible  
 578 malfunctioning channels and, eventually, restore them through  
 579 a recovery procedure.

580 The slow controls and monitoring of the RICH detector  
 581 is enforced by the hardware interlock system based on the  
 582 National Instruments CompactRIO (cRIO) [23]. The cRIO  
 583 system monitors the following parameters:

- 584 • Temperature and humidity in 16 locations of the detector  
 585 volume;
- 586 • Temperature and humidity in 16 locations of the electron-  
 587 ics panel;
- 588 • Air tank pressure;
- 589 • Air and nitrogen flow.

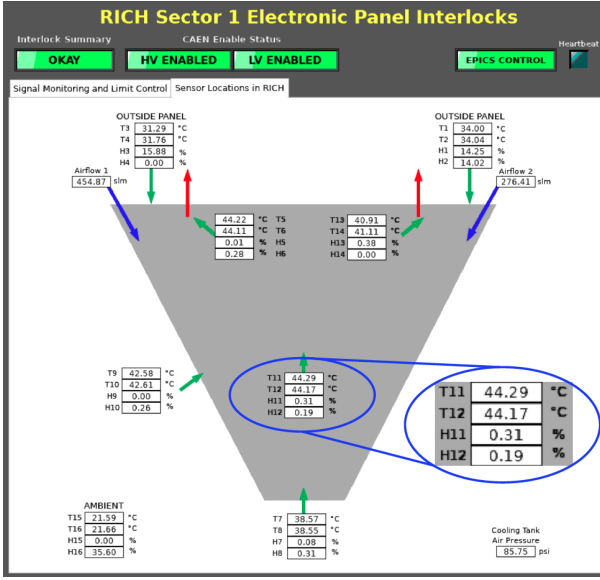


Figure 31: Location and measured values of the temperature and humidity sensors inside the electronics panel, and the cooling air input flow as measured by the flow meters of the gas line.

690 The locations of the temperature and humidity sensors, and  
 691 the air and nitrogen flows fed into the electronics panel and  
 692 nitrogen volume are shown in Figs. 31 and 32, respectively.  
 693 The inner temperature of the electronics panel ranges between<sup>723</sup>  
 694 38.5°C and 44.5°C moving from the bottom towards the top<sup>724</sup>  
 695 of the module, whereas the external temperature stays below  
 696 34.5°C, in accordance with the requirement to not drive the<sup>725</sup>  
 697 FTOF system above 40°C. The relative humidity is below 0.5%.  
 698 In the nitrogen volume, the temperature ranges between 23°C<sup>726</sup>  
 699 and 27°C. The relative humidity is below 1.3% except in the<sup>727</sup>  
 700 central point close to the spherical mirror pivot, where it reaches<sup>728</sup>  
 701 a 3% value.<sup>729</sup>

702 The signal levels are controlled by setting limits. If the<sup>730</sup>  
 703 temperatures, air flow, or air pressure go out of limits, the HV<sup>731</sup>  
 704 and LV are powered off, i.e. interlocked. In case the humidity or<sup>732</sup>  
 705 the nitrogen flow are out of limits, an alarm signal is generated.<sup>733</sup>

706 Important safety parameters of the RICH detector are: the<sup>734</sup>  
 707 temperature of the front-end electronics, the gas flow, and the<sup>735</sup>  
 708 RICH internal relative humidity. Figure 33 presents the map of<sup>736</sup>  
 709 the temperatures of the front-end electronics. Typical tempera-<sup>737</sup>  
 710 ture values are around 65°C on the FPGA chips and 40°C inside<sup>738</sup>  
 711 the electronics panel volume. The safety temperature limits<sup>739</sup>  
 712 are 85°C for the FPGAs, 80°C for the optical fiber cables, and<sup>740</sup>  
 713 40°C for the temperature on the FTOF detector, which is about<sup>741</sup>  
 714 10 cm away from the RICH. Therefore, the maximum allowed<sup>742</sup>  
 715 temperature was set to 75°C on the FPGA and to 45°C inside<sup>743</sup>  
 716 the electronics panel volume.<sup>744</sup>

717 The nitrogen flow and the RICH internal relative humidity<sup>745</sup>  
 718 are measured by several probes installed inside the detector. An<sup>746</sup>  
 719 alarm is sent out in case the humidity exceeds 5% or in case<sup>747</sup>  
 720 the nitrogen flow drops below the normal value. In the latter<sup>748</sup>  
 721 case, the backup system starts working to restore the normal<sup>749</sup>  
 722 flow level and to ensure safe humidity conditions. During RICH<sup>750</sup>

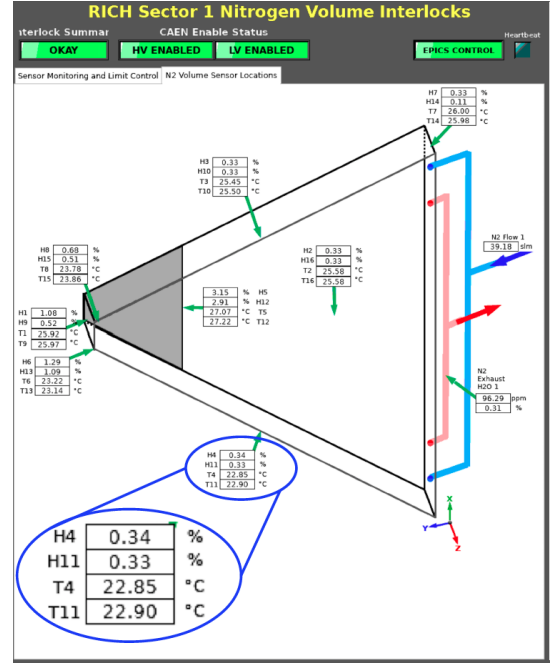


Figure 32: Location and measured values of the temperature and humidity sensors inside the nitrogen volume, and the nitrogen input flow as measured by the flow meters of the gas line.

operation, the humidity level has proven to be very stable with time.

## 5. The Initial Performance of the RICH Detector

### 5.1. RICH Event Reconstruction

The RICH reconstruction is organized in four steps. In the first step, the spatial and time information of each hit in the MaPMTs is corrected by the spatial misalignment and time calibration parameters. The hits are ordered as a function of their ToT value, as this reflects the corresponding amplitude (released charge). A 3×3 MaPMT pixel matrix centered around a local maximum, i.e. the hit with the highest local ToT, is called a nonet. If more than 3 hits are found in the same nonet they are grouped into a RICH cluster. A cluster is typically generated by a charged particle producing Cherenkov light in the MaPMT window or ionization in the sensor dynode structure. If a sole hit is found close to a local maximum with a ToT lower than 80% of that maximum, the hit is flagged as possible cross-talk. Hits belonging to the same nonet of the local maximum are flagged as optical cross-talk, while hits readout by an electronics channel adjacent to the maximum hit in the MAROC chip are flagged as electrical cross-talk. Note that the readout circuit routing has been designed to connect anodes close in space to non-adjacent MAROC3 inputs. The above selection rejects about 87% of the cross-talk hits, as can be seen in Fig. 34. In the figure, the ToT distribution of the recorded RICH hits (black solid line) is shown together with the distributions of the hits identified as optical (magenta dash-dotted line) or electrical (green dashed line) cross-talk.

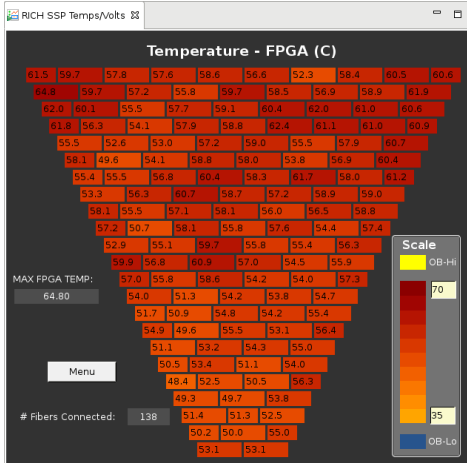


Figure 33: Slow controls display: Map of the temperatures measured on the FPGA chips.

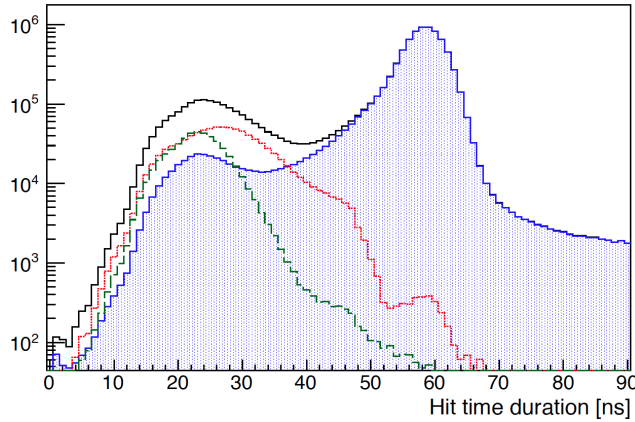


Figure 34: ToT distribution of the recorded RICH hits (black solid line) together with the optical (magenta dash-dotted line) and electrical (green dashed line) cross-talk distributions. The hits selected for further analysis are highlighted by the blue dotted histogram.

The shoulders on the right of the cross-talk peaks are likely due to signal discharges wrongly identified as cross-talk. The hits selected for further analysis are highlighted by the dotted (blue) histogram. The excess at low ToT values indicates residual contamination of unidentified cross-talk. The leftover cross-talk contamination, at the level of 2.7% of the signal, can be further reduced only with a time versus amplitude analysis, see Section 5.2. The cross-talk selection also removes a small (0.8% fraction) of true Cherenkov signals. Those correspond to MaPMT discharges that undergo incomplete dynode multiplication, while being by chance close in space to another Cherenkov signal. Hits flagged as cross-talk are not considered further in the RICH reconstruction.

The second step consists in finding the spatial match between the RICH clusters and the CLAS12 charged particle tracks. This requires that the extrapolated impact point of the track on the MaPMT plane is within 10 cm of the cluster center. The latter is calculated as a weighted average - with the ToT

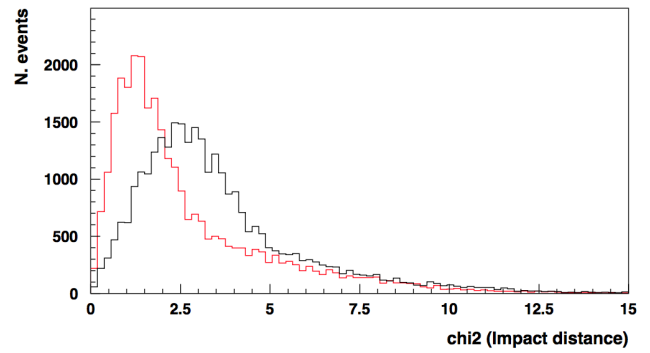


Figure 35: RICH matching  $\chi^2$ , defined as the distance between the RICH clusters and the matched drift chamber tracks divided by the pixel spatial RMS. The black distribution is before and the red one is after the alignment procedure.

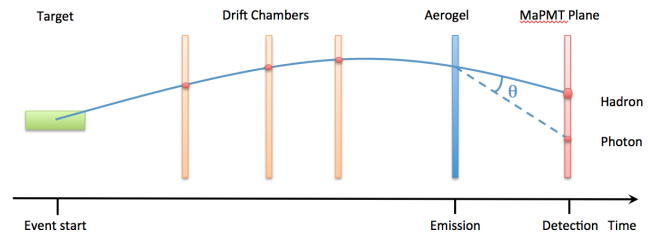


Figure 36: The RICH photon detection time as measured by the CLAS12 spectrometer. It is defined as the event start time plus the flight-times of the hadron from the interaction point to the radiator center and of the ray-traced photon within the RICH volume.

value as the weight - of the spatial coordinates of all the hits in the cluster. Matched clusters allow a precise study of the MaPMT detector position and orientation relative to the CLAS12 tracking system. This is shown in Fig. 35, where the distance between the RICH clusters and the matched drift chamber tracks [24] divided by the pixel spatial RMS, a sort of  $\chi^2$  distribution, is reported. The black distribution is before and the red one is after the alignment procedure.

The third step is the core of the RICH reconstruction [25]. For each hit in the MaPMT plane, an estimate of the corresponding Cherenkov angle is derived by ray-tracing the photon path inside the RICH volume taking into account possible reflections. This is done in turn for each charged particle traced through the RICH, with the photon emission point assumed to be the middle point of the particle path inside the aerogel radiator. In the fourth step, a particle identification algorithm is applied using an event-based likelihood of the reconstructed Cherenkov angles and times.

## 5.2. RICH Time Resolution

The time information of the RICH hits is provided by the leading edge time  $T_1$  measured by the TDC implemented into the FPGA board with a 1-ns precision. In-time photon hits are selected by comparing their  $T_1$  with the time  $T_{calc}$  computed using the CLAS12 information (see Fig. 36).  $T_{calc}$  comprises the event start time, the charged track path and flight time provided by the tracking system, and the Cherenkov photon

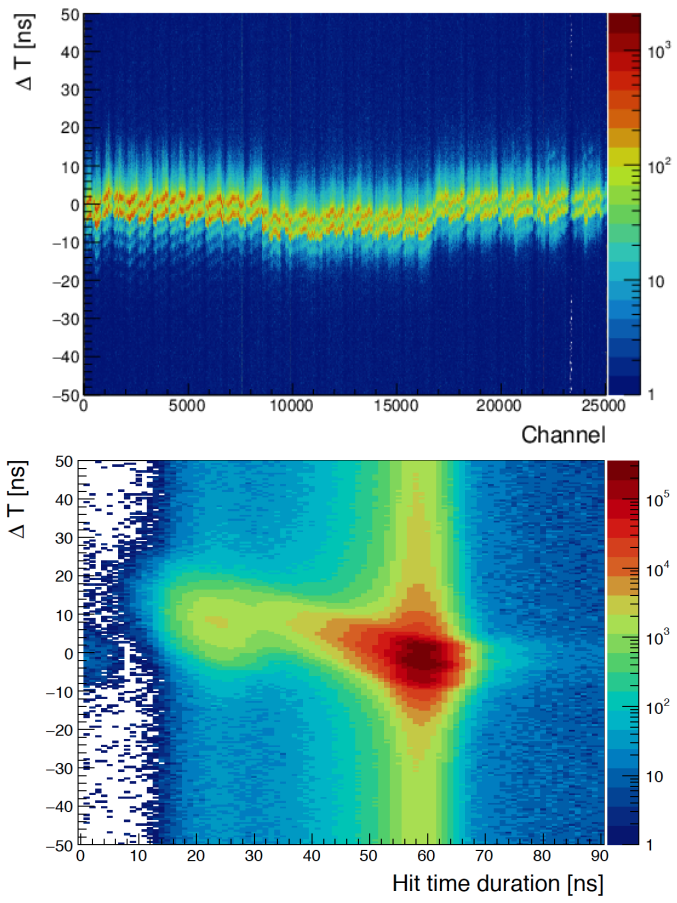


Figure 37: Top plot: distribution of the time difference  $\Delta T$  between the measured RICH and calculated CLAS12 times as a function of the RICH readout channel. Bottom plot: cumulative distribution of the time difference  $\Delta T$  as a function of the hit duration time (ToT).

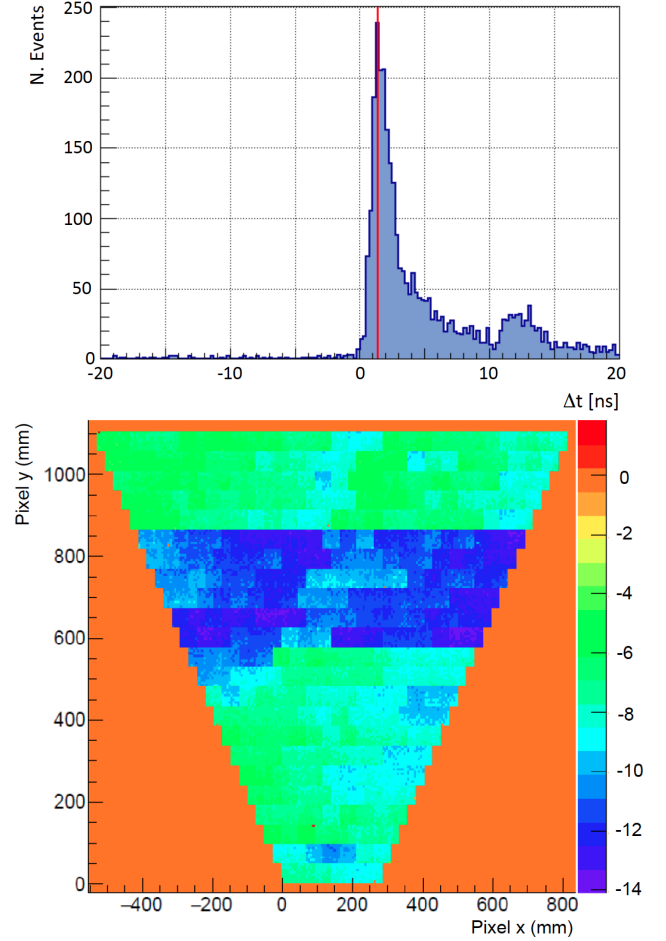


Figure 38: Top plot:  $\Delta T$  distribution for one readout channel; the red line indicates the time offset value. Bottom plot: typical map of the time offsets.

path reconstructed inside the RICH as explained in Ref. [25].<sup>817</sup>  
 Being based on the precise FTOF system [3] and the accelerator<sup>818</sup>  
 RF frequency, the CLAS12 computed time features a time<sup>819</sup>  
 resolution on the order of 100 ps, significantly better than<sup>820</sup>  
 RICH. The CLAS12 computed time can therefore be used as<sup>821</sup>  
 a reference for the RICH time calibration.<sup>822</sup>

With respect to the expected time resolution, significant<sup>823</sup>  
 channel-by-channel variations are found in the difference be-<sup>824</sup>  
 tween the measured and the calculated times as shown in the<sup>825</sup>  
 top plot of Fig. 37, where the distribution of  $\Delta T = T_1 - T_{calc}$  as<sup>826</sup>  
 a function of the channel number is shown. These variations are<sup>827</sup>  
 introduced by the readout chain, with the biggest contribution<sup>828</sup>  
 coming from the average length of the 3 optical DAQ fiber<sup>829</sup>  
 trunks and from the specific length of the various fibers in each<sup>830</sup>  
 trunk. Smaller variations among the individual channels of one<sup>831</sup>  
 board can also occur due to the different circuit routing and<sup>832</sup>  
 components. An additional overall time constant is expected<sup>833</sup>  
 from the relative calibration of the RICH with respect to the<sup>834</sup>  
 rest of the CLAS12 detectors.<sup>835</sup>

A broadening of the  $\Delta T$  distributions is due to the time walk,<sup>836</sup>  
 i.e. the dependence of the trailing edge time on the amplitude<sup>837</sup>  
 of the input signal. Since the MAROC3 readout mostly works<sup>838</sup>

in the saturated regime already at the SPE level, this effect is expected to be relevant for small amplitude signals, as can be seen from the bottom plot of Fig. 37. Saturated signals have typical ToT values on the order of 60 ns, while small amplitude signals are expected to be discriminated up to several ns later. The vertical band at  $ToT \approx 60$  ns comprises a distribution of random-time MaPMT dark counts and off-time beam bunches. The independent excess around  $ToT \approx 25$  ns signals a residual contamination of cross-talk pulses as anticipated in Section 5.1.

A two-step calibration procedure was implemented in order to align the time measured from all RICH readout channels with the expected (calculated) one. The current version of the software uses electrons and charged pions identified in CLAS12 with momenta larger than 2.5 GeV and Cherenkov photons reconstructed in the RICH with no reflections on the mirrors.

The first step of the procedure consists in the evaluation of the 25024 time offset corrections. The values of  $\Delta T$  are plotted for each channel and the position of the maximum is taken as the time offset for that channel. The top plot of Fig. 38 shows a typical  $\Delta T$  distribution, with a pronounced peak, a broad tail due to the time walk, and a small enhancement above  $\approx 10$  ns most likely due to residual cross-talk hits. The vertical

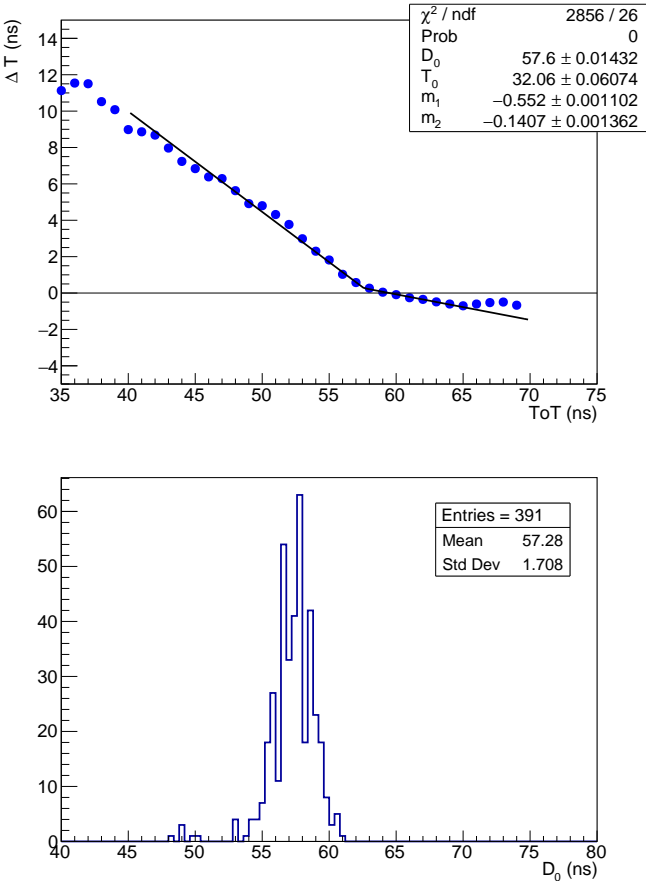


Figure 39: Top plot: fit of the time-walk correction for one MaPMT. Bottom plot: distribution of the ToT saturation values extracted from the time-walk corrections.

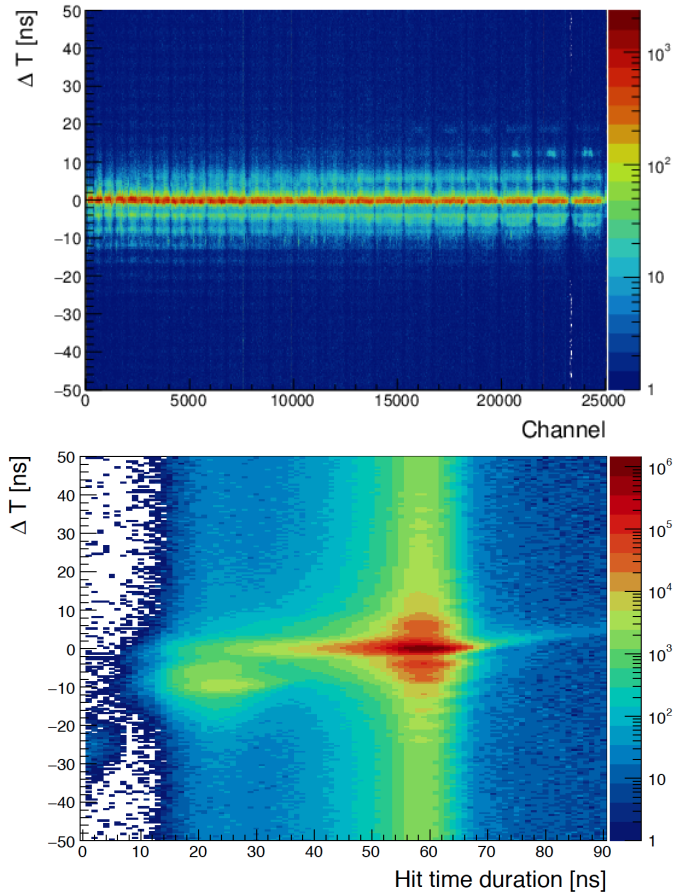


Figure 40: Distribution of the time difference  $\Delta T$  between the measured RICH and extrapolated CLAS12 times after the time calibration. On the top as a function of the readout channel; on the bottom as a function of the signal amplitude ToT.

line indicates the adopted value for the time offset correction.<sup>861</sup>  
 The bottom plot of Fig. 38 shows a typical map of the time<sup>862</sup>  
 offsets. Three regions of comparable values are highlighted,<sup>863</sup>  
 corresponding to the tiles connected to the 3 optical fiber trunks,<sup>864</sup>  
 on top of smaller channel-by-channel variations.<sup>865</sup>

Once the individual channels were corrected for the time<sup>866</sup>  
 offsets, the time-walk corrections were extracted from the  $\Delta T$ <sup>867</sup>  
 distribution as a function of ToT. Since the threshold level<sup>868</sup>  
 is common to all channels of one MAROC3 chip, and the<sup>869</sup>  
 amplitude equalization has been performed, one expects that<sup>870</sup>  
 the same time-walk correction should work for all channels<sup>871</sup>  
 of one MaPMT. This was verified by comparing plots like the<sup>872</sup>  
 one shown in the bottom plot of Fig. 37 for all channels of the<sup>873</sup>  
 MaPMTs. A set of 391 time-walk correction functions, one per<sup>874</sup>  
 MaPMT, is therefore extracted by fitting the dependence of  $\Delta T$ <sup>875</sup>  
 as a function of ToT, as shown in the top plot of Fig. 39. The<sup>876</sup>  
 dependence is fit with two lines, one for the saturated regime<sup>877</sup>  
 and one for the linear region. The free parameters of the fit  
 are the two slopes, the ToT value where the two lines cross,<sup>878</sup>  
 i.e. the saturation ToT, and the  $\Delta T$  at zero ToT. The data show  
 small deviations from the linear behavior. However, such a<sup>879</sup>  
 simple functional form was adopted to minimize the probability<sup>880</sup>

of fit failure (having to deal with several hundreds of fits) and because it was proven to be enough to achieve time resolutions that meet the specifications. In the bottom plot of Fig. 39, a typical distribution of the saturation ToT values obtained from the fit is shown. The average value is around 57 ns with small variation from MaPMT to MaPMT.

After calibration, the corrected  $\Delta T$  distribution is centered at zero for all channels, see Fig. 40. As a consequence, a few ns time coincidence can be applied to remove the spurious hits. As shown in the bottom panel of Fig. 40, the cross-talk hits at  $ToT \approx 25$  ns and the 4.008 ns sub-structure of the off-time beam bunches at  $ToT \approx 60$  ns become clearly visible. A typical  $\Delta T$  distribution is shown in Fig. 41, where the red and black histograms show the  $\Delta T$  values before and after the correction, respectively. The red curve is a Gaussian fit of the corrected distribution. On average, we obtained a time resolution  $\langle \sigma \rangle \approx 0.7$  ns, well below the requirement of 1 ns.

### 5.3. RICH Hadron Separation

The RICH has been designed to provide hadron identification in the 3 - 8 GeV momentum range. The most challenging

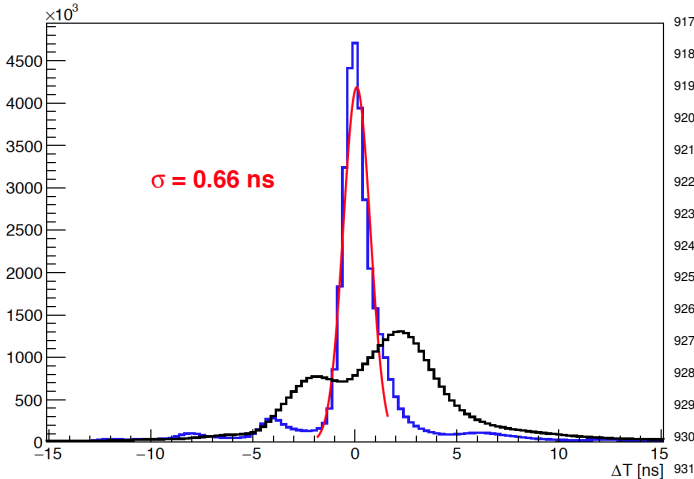


Figure 41: Typical  $\Delta T$  distribution before (black) and after (blue) the time-walk correction for all RICH pixels. The red line is a Gaussian fit of the corrected distribution, with a global width  $\sigma=0.66$  ns

photon flight time within the RICH (photon transit time). The time coincidence  $\Delta T$  should be close to zero for any true photon path. As a consequence, a valid photon reconstruction is initially selected by requiring  $\Delta T < 3$  ns, indicated by the horizontal dashed lines. The path length is represented by the photon transit time inside the RICH, from the emission point within the aerogel to the detection point in the MaPMT plane after all possible reflections. Photons reflected by the spherical mirror and directed back to the aerogel travel twice the gap, with an expected significant increase of path length and a corresponding distinctive  $\approx 6$  ns longer transit time.

In the bottom panel, the measured angles are compared to the expected distributions for different particle hypotheses. The width of each distribution corresponds to the expected SPE angular resolution, while the average value depends on the particle type and momentum. An acceptance range is defined from the smallest angle expected for a proton to the largest angle expected for an electron, enlarged by three times the expected angular resolution. For the latter, a conservative value of 6 mrad is taken for the single photon case. These limits are indicated by the vertical dashed lines.

For each reconstructed photon path an estimate of the corresponding Cherenkov angle is obtained and histogrammed on the plot. In all cases studied, both reflected and direct photon information is consistent with the electron hypothesis. In particular, the reconstructed reflected and direct photon paths with  $\Delta T$  close to zero provide Cherenkov angle values consistent with an electron, as expected. The narrow distribution of the measured angle values indicate that kaons can clearly be separated up to momenta greater than 6 GeV. Electrons can be distinguished from pions only at low momenta, below 2 GeV.

Each aerogel tile presents specific features because the challenging production process, tuned to achieve the highest transparency over a large volume, is not fully industrialized. The most important quality parameters are the density, related to the average refractive index, homogeneity, related to the refractive index variations within the volume, and tile bending, originated by the inner material tension and related to the surface planarity. The effect of these features on the RICH photon reconstruction can be studied in detail using the control sample of electrons identified by CLAS12. Given the large number of tiles and the broad range of particle directions after the CLAS12 bending magnets, such a study requires large statistics and is still ongoing. A similar approach is used for the alignment study. Also in this case, large statistics are needed due to the numerous involved components (aerogel layers, mirrors, and MaPMT plane) and photon path configurations.

As a general approach, the RICH performance is studied separately for each aerogel tile. The RICH global performance estimators are then defined by averaging the results over all the radiator tiles. Despite the fact that the above studies have not yet been finalized, and only partial corrections have been implemented so far, the preliminary SPE Cherenkov angle resolution yields typical values around 6 mrad. It is expected to improve towards the goal value of 4.5 mrad once the corrections for the detector misalignment are implemented and the realistic optical parameters of each aerogel tile are taken into account.

separation is between kaons and pions, as their Cherenkov angles become closer and closer with the increase of momentum until a minimum difference of 6 mrad at 8 GeV. In addition, in this momentum range the pion yield is more than an order of magnitude larger than for the other hadron species.

Various ring imaging topologies are possible due to the unconventional RICH geometry. These topologies are generated by direct photons in proximity focusing and by reflected photons in mirror focusing geometries. In the momentum range of interest (between 3 GeV and 8 GeV), electrons can be used for a detailed optimization of the RICH performance since, being in a saturated regime, their Cherenkov angles are indistinguishable from those of pions. The work is still ongoing to make use of the large recorded electron statistics.

Examples of reconstructed RICH events are shown in Figs. 42 to 45 for particles identified as electrons by CLAS12. In each figure, the reconstructed RICH event is displayed on the left. The ray-tracing approach allows, for each particle hypothesis, to anticipate the expected photon pattern and the associated hits on the photodetectors, indicated by the small dots in the figures. The measured RICH hits are shown as open circles, whereas the reconstructed photon hits are shown as full symbols. Direct and reflected photons are indicated in magenta circles and blue squares, respectively. A remarkable feature of the RICH detector is the low level of spurious hits from accidentals, in-time background (i.e. Rayleigh scattering), and dark counts. This feature is crucial for the most challenging cases: particles with high momenta close to the 8 GeV limit that require the best resolution in Cherenkov angle, and particles pointing towards the spherical mirror whose number of detected photons is limited by the double reflection and a second passage through the radiator.

For each event, the details of the time and Cherenkov angle reconstruction are shown on the right. On the top panel, the time coincidence  $\Delta T$  between the RICH measured hit and the CLAS12 calculated time is displayed as a function of the

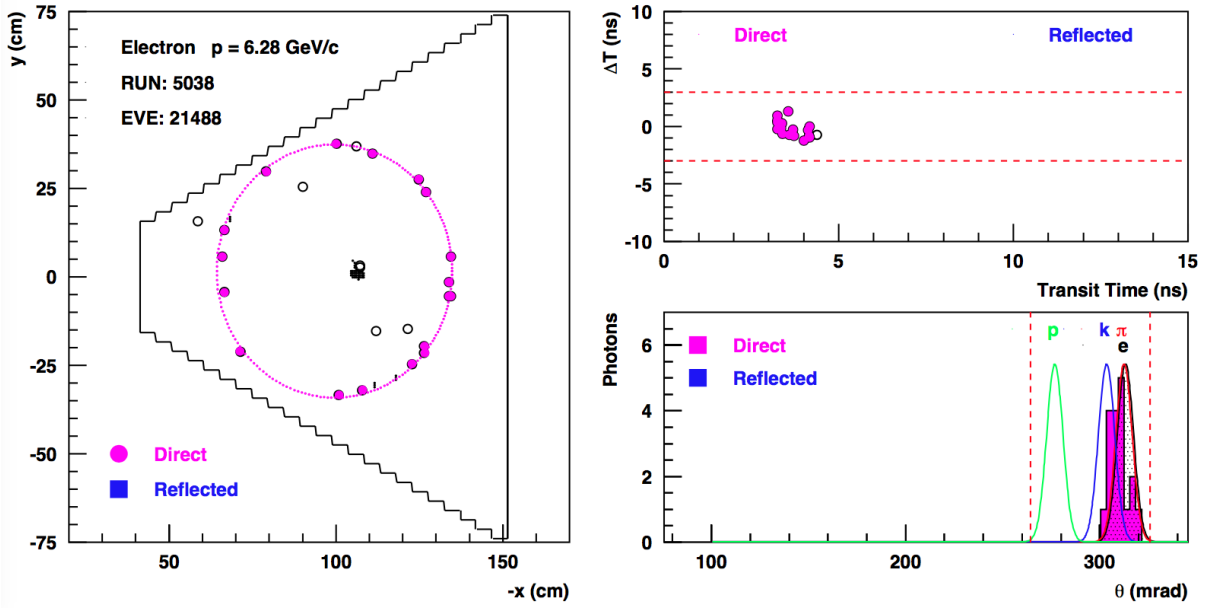


Figure 42: Example of a reconstructed RICH event with only direct photons. On the left the event display, on the right the time (top) and angle (bottom) analysis. Refer to the text for details.

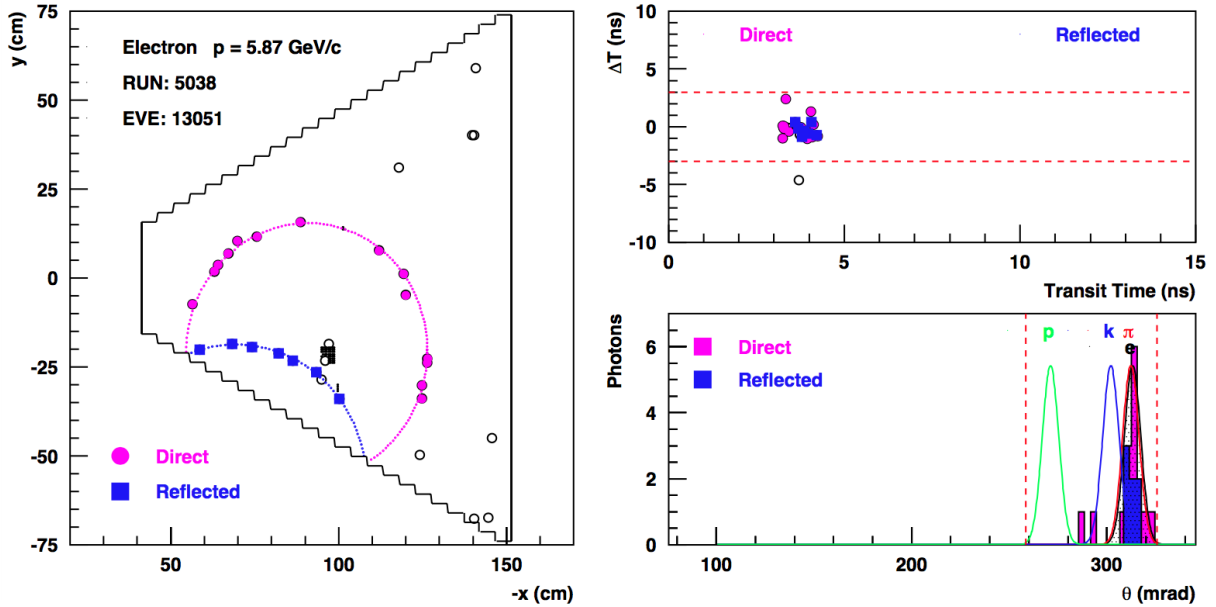


Figure 43: Example of a reconstructed RICH event with a partial ring reflected by the lateral flat mirror. On the left the event display, on the right the time (top) and angle (bottom) analysis. Refer to the text for details.

As an example, the effect of a preliminary alignment of the RICH as a whole is shown for one aerogel tile in Fig. 46. The resolution is calculated as the RMS of the distribution of the average Cherenkov angles extracted for each single track of the electron control sample. Such averages are calculated over the detected photons, whose reconstructed path satisfies the time coincidence and provides an angle within the kinematic limits described above, associated with the track. The fit shown uses

the function

$$\sigma = \sqrt{\frac{\sigma_1^2}{N} + \sigma_0^2}$$

<sup>974</sup> to extract the single photon resolution  $\sigma_1$  in addition to a constant term  $\sigma_0$  measuring the residual systematics due, e.g. to misalignment. After (a preliminary) alignment, the resolution improves toward the design values, which are 4.5 mrad for <sup>975</sup> single photon detection and 1.5 mrad for the average over all the <sup>976</sup> <sup>977</sup> <sup>978</sup>

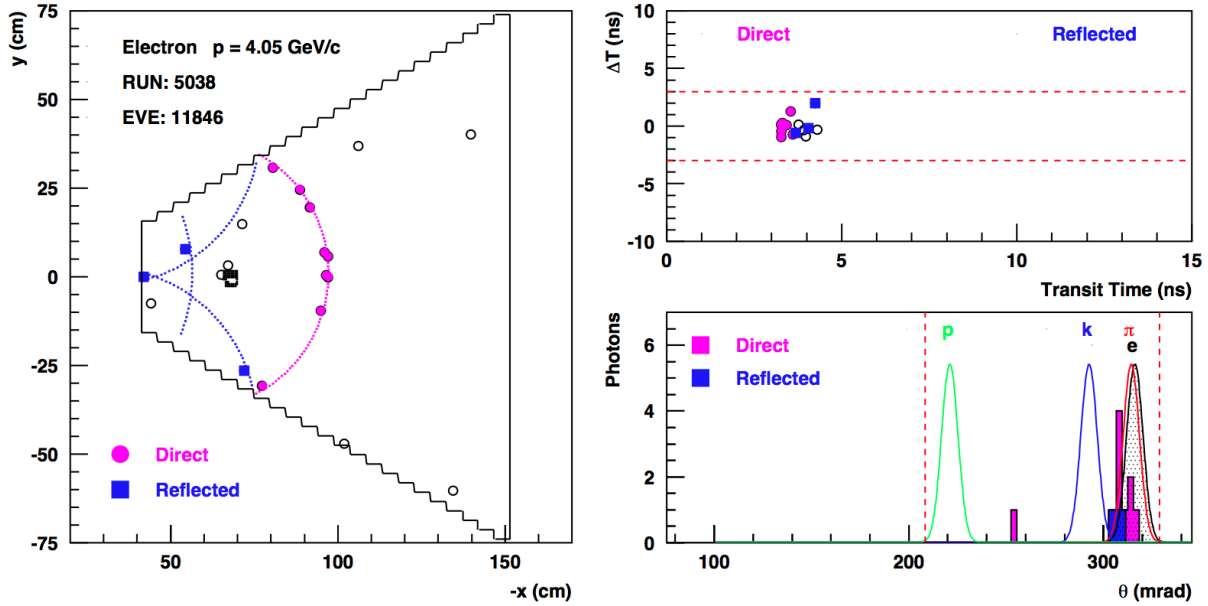


Figure 44: Example of a reconstructed RICH event with photons reflected by all the lateral mirrors. On the left the event display, on the right the time (top) and angle (bottom) analysis. Refer to the text for details.

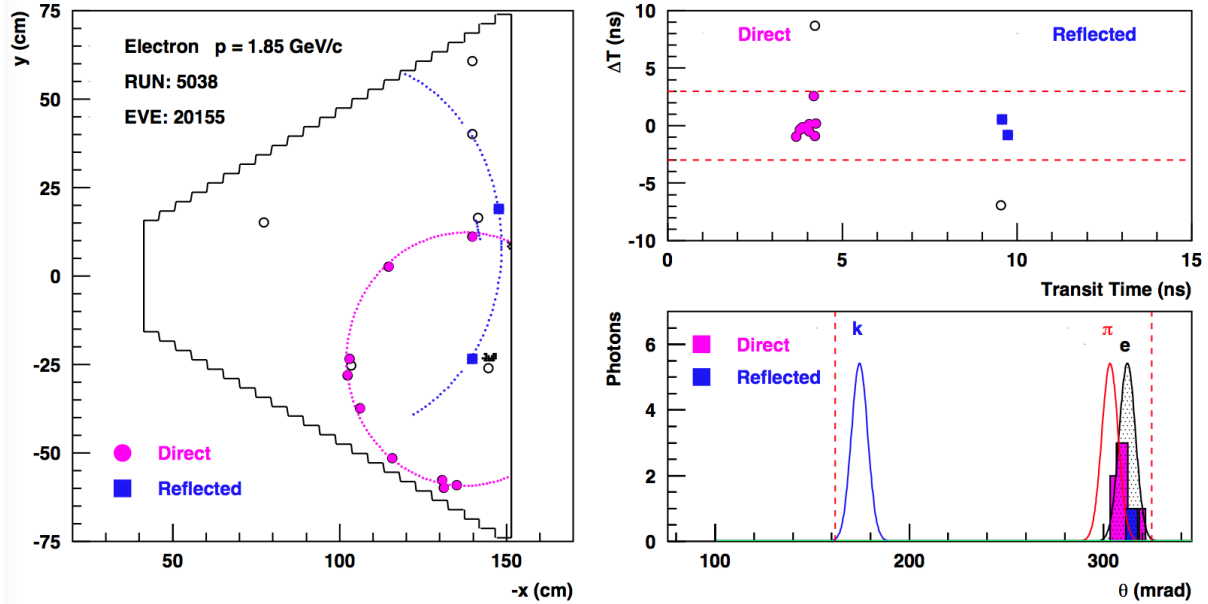


Figure 45: Example of a reconstructed RICH event with a partial ring reflected back by the spherical mirror and passing twice the aerogel layer. On the left the event display, on the right the time (top) and angle (bottom) analysis. Refer to the text for details.

979 photons that are associated with the control electron track. Such preliminary Cherenkov angle resolution is already sufficient for an effective hadron separation in the goal range of momenta, from 3 to 8 GeV, as shown by Figs. 47 to 49.

## 983 6. Conclusions

984 A RICH detector has been designed to enhance the hadron identification capability at CLAS12 in the 3 to 8 GeV mo-

986 momentum range. It substitutes the baseline LTCC gas threshold Cherenkov detector in two of the CLAS12 sectors, to create a symmetric left-right setup optimized for running with polarized targets. The first module was installed at the beginning of 2018, in time for the start of the experiment data taking. The second module is under construction and expected to be ready in the summer 2021, in time for the first run with polarized targets.

989 990 991 992 To efficiently cover the desired few-GeV momentum range, the RICH employs innovative technological solutions. Among

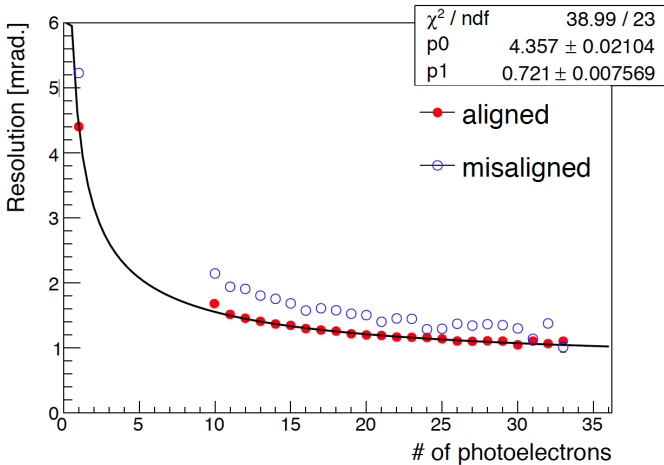


Figure 46: RICH Cherenkov resolution before (open points) and after (solid points) a preliminary RICH alignment. The whole RICH detector is aligned minimizing the matching distance between the RICH clusters and the extrapolated drift chamber tracks. No possible misalignment of a single RICH component is accounted for. The distribution is for particles passing through one aerogel tile of 2-cm thickness (tile 12 in layer 1) and for direct photons.

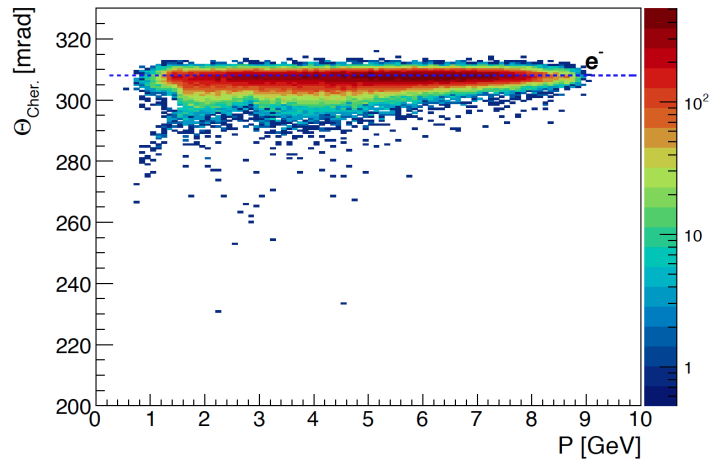


Figure 47: RICH response for electrons as identified by CLAS12. As expected, the measured Cherenkov angle is saturated over the whole momentum range, from 3 GeV up to 8 GeV. The distribution is for particles passing through one aerogel tile of 2-cm thickness (tile 12 in layer 1) and direct photons.

these are composite aeronautic light-materials to ensure the needed mechanical structure rigidity, aerogel radiators of unprecedented large volume (up to  $200 \times 200 \times 30 \text{ mm}^3$ ) and high transparency ( $\approx 50 \text{ mm}$  scattering length), light mirrors (of the order of 1% radiation length) made of carbon fiber or, for the first time in a nuclear experiment, glass-skin technology, and highly segmented and highly packed Hamamatsu H8500 and H12700 multi-anode photomultipliers. A compact and scalable readout electronics system has been realized for the detector able to discriminate Cherenkov signals down to as small as a 1/32 fraction of the single photon amplitude, with excellent efficiency and stability, and a time resolution better than 1 ns.

The peculiar geometry of the CLAS12 sector suggested a innovative hybrid-optics solution to limit the active area per sector, with part of the light directly imaged and part of the light detected after reflection from mirrors. This and the bending into the torus field of the CLAS12 Forward Detector create a variety of possible topologies for the particle and photons paths. The RICH reconstruction exploits a ray-tracing algorithm to provide a Cherenkov angle estimation for each photon hit and hadron track in the event. This basic experimental information allows an independent development of higher-level PID algorithms with increasing sophistication.

Preliminary data analysis shows that the CLAS12 RICH is able to match the required time and Cherenkov angle resolutions. After calibration, each of the 25k channels features a time resolution of the order of 0.6 ns, better than the 1 ns specification. High-momentum particles define the most stringent requirements for the RICH performance. As the pion yield is larger than the other particles species by an order of magnitude, a  $4\sigma$  angle separation is required to contain the contamination at the percent level. At 8 GeV, this implies an angle resolution of 1.5 mrad. Despite the fact that the detailed study of the alignment and optical performance

of the various components is still ongoing, the detector has already demonstrated a single-photon angle resolution better than 5 mrad and an average number of 19 photons per charged particle in the forward high-momentum direction, in line with the detector design specifications. This reflects in an angle resolution per charged particle close to the design value of 1.5 mrad and an effective hadron identification capability over the entire required momentum range.

## 7. Acknowledgments

This material is based upon work supported by INFN under the MIUR priority project CLASMED, Italy and by the U.S. Department of Energy, Office of Science, Office of Nuclear Physics under contract DE-AC05-06OR23177 and the National Science Foundation, Award #1615067. We thank the JLab Detector Support Group and Fast Electronics Group, the Hall B technical and management staff, and the INFN technical and administrative service.

## References

- [1] Y. Sharabian *et al.*, “The CLAS12 High Threshold Cherenkov Counter”, to be published in Nucl. Inst. and Meth. A, (2020). (see this issue)
- [2] M. Ungaro *et al.*, “The CLAS12 Low Threshold Cherenkov Counter”, to be published in Nucl. Inst. and Meth. A, (2020). (see this issue)
- [3] D.S. Carman *et al.*, “The CLAS12 Forward Time-of-Flight System”, to be published in Nucl. Inst. and Meth. A, (2020). (see this issue)
- [4] V.D. Burkert *et al.*, “The CLAS12 Spectrometer at Jefferson Laboratory”, to be published in Nucl. Inst. and Meth. A, (2020). (see this issue)
- [5] G. Asryan *et al.*, “The CLAS12 Forward Electromagnetic Calorimeter”, to be published in Nucl. Inst. and Meth. A, (2020). (see this issue)
- [6] M. Contalbrigo *et al.*, “The Large-Area Hybrid-optics CLAS12 RICH Detector: Tests of Innovative Components”, Nucl. Inst. Meth. **A766**, 22 (2014).
- [7] M. Contalbrigo *et al.*, “Aerogel mass production for the CLAS12 RICH: Novel characterization methods and optical performance”, Nucl. Inst. Meth. **A876**, 168 (2017).

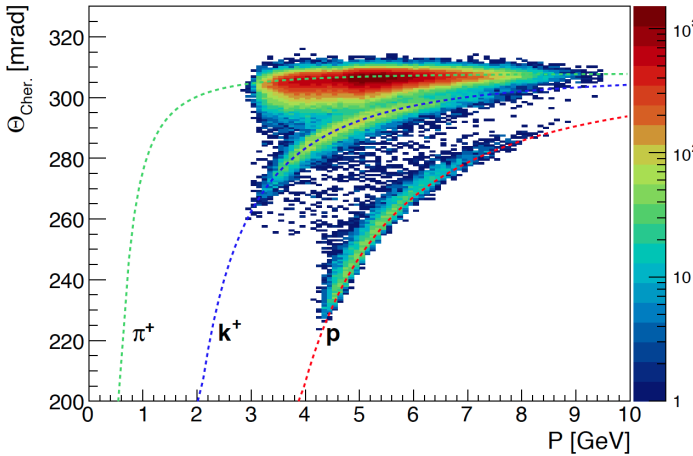


Figure 48: RICH response for non-electron particles as defined by CLAS12. The measured Cherenkov angles distribute around the expected values for pion, kaon, and proton hypotheses as a function of their momentum. The three hadron populations are separated over the whole momentum range, from 3 GeV up to 8 GeV. The distribution is for particles passing through one aerogel tile of 2-cm thickness (tile 12 in layer 1) and spanning the entire momentum range of interest for RICH.

- 1063 [8] E. Aschenauer *et al.*, “Optical Characterization of  $n = 1.03$  Silica Aerogel  
1064 used as Radiator in the RICH of HERMES”, Nucl. Inst. Meth. A **440**, 338  
1065 (2000).
- 1066 [9] <http://www.compositemirrors.com/>.
- 1067 [10] G.J. Barber *et al.*, “Development of Lightweight Carbon-Fiber Mirrors  
1068 for the RICH 1 Detector of LHCb”, Nucl. Inst. Meth. A **593**, 624 (2008).
- 1069 [11] <https://www.evaporatedcoatings.com/>.
- 1070 [12] <http://www.media-lario.com/>.
- 1071 [13] [https://www.hamamatsu.com/resources/pdf/etd/H8500\\_H10966 TPMH1327E.pdf](https://www.hamamatsu.com/resources/pdf/etd/H8500_H10966 TPMH1327E.pdf).
- 1072 [14] R. A. Montgomery *et al.*, “Multianode Photomultiplier Tube Studies for  
1073 Imaging Applications”, Nucl. Inst. Meth. A **695**, 326 (2012).
- 1074 [15] S. Anefalos Pereira *et al.*, “Test of the CLAS12 RICH Large Scale  
1075 Prototype in the Direct Proximity Focusing Configuration”, Eur. Phys.  
1076 J. A **52**, 23 (2016).
- 1077 [16] <https://www.hamamatsu.com/resources/pdf/etd/H12700 TPMH1348E.pdf>.
- 1078 [17] M. Contalbrigo *et al.*, “Single Photon Detection with the Multi-  
1079 anode CLAS12 RICH Detector”, in press in Nuc. Inst. Meth. A.,  
1080 DOI:10.1016/j.nima.2019.04.077
- 1081 [18] S. Blin *et al.*, “MAROC, a Generic Photomultiplier Readout Chip”, IEEE  
1082 Nucl. Sci. Symp. Conf. Rec. 2010, 1690 (2010).
- 1083 [19] S. Boyarinov *et al.*, “The CLAS12 Data Acquisition System”, to be  
1084 published in Nucl. Inst. and Meth. A, (2020). (see this issue)
- 1085 [20] Pavel Deltarenko, “Precision Analysis of the Photomultiplier Response  
1086 to Ultra Low Signals”, Nucl. Inst. Meth. A **872**, 1 (2017).
- 1087 [21] P. Deltarenko, V. Kubarsky, A. Kim, and A. Smith, to be published.
- 1088 [22] Experimental Industrial Physics Control System, <https://epics-controls.org>
- 1089 [23] [https://www.jlab.org/div\\_dept/physics\\_division/dsg/notes/2016-012%20National%20Instruments%20compactRIO-based%20control,%20monitoring,%20and%20interlock%20system.pdf](https://www.jlab.org/div_dept/physics_division/dsg/notes/2016-012%20National%20Instruments%20compactRIO-based%20control,%20monitoring,%20and%20interlock%20system.pdf)
- 1090 [24] M.D. Mestayer *et al.*, “The CLAS12 Drift Chamber System”, to be  
1091 published in Nucl. Inst. and Meth. A, (2020). (see this issue)
- 1092 [25] V. Ziegler *et al.*, “The CLAS12 Software Framework and Event Recon-  
1093 struction”, to be published in Nucl. Inst. and Meth. A, (2020). (see this  
1094 issue)
- 1095
- 1096
- 1097
- 1098
- 1099
- 1100

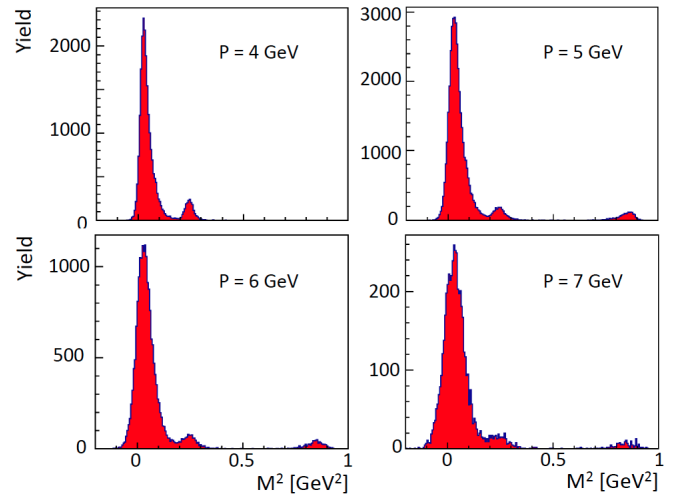


Figure 49: RICH response for non-electron particles in slices of momentum, from 4 GeV up to 7 GeV.